

An analysis of the far-field response to external forcing of a suspension in Stokes flow in a parallel-wall channel

J. Bławdziewicz

Department of Mechanical Engineering, Yale University, P.O. Box 20-8286, New Haven, CT 06520

E. Wajnryb

IPPT, Świętokrzyska 21, Warsaw, Poland

(Dated: August 13, 2008)

The leading-order far-field scattered flow produced by a particle in a parallel-wall channel under creeping flow conditions has a form of the parabolic velocity field driven by a 2D dipolar pressure distribution. We show that in a system of hydrodynamically interacting particles, the pressure dipoles contribute to the macroscopic suspension flow in a similar way as the induced electric dipoles contribute to the electrostatic displacement field. Using this result we derive macroscopic equations governing suspension transport under the action of a lateral force, a lateral torque or a macroscopic pressure gradient in the channel. The matrix of linear transport coefficients in the constitutive relations linking the external forcing to the particle and fluid fluxes satisfies the Onsager reciprocal relation. The transport coefficients are evaluated for square and hexagonal periodic arrays of fixed and freely suspended particles, and a simple approximation in a Clausius-Mossotti form is proposed for the channel permeability coefficient. We also find explicit expressions for evaluating the periodic Green's functions for Stokes flow between two parallel walls.

I. INTRODUCTION

There have been numerous studies of the effect of confinement on the dynamics of rigid particles [1–8], deformable drops [9–12], and macromolecules [13, 14] in creeping flow in a parallel-wall channel. The investigations revealed new confinement-induced phenomena such as migration of macromolecules away from the walls [13, 15–17], stability of strongly elongated drops in a confined shear flow [9, 10, 12], and cross-streamline migration of spherical particles due to pair encounters in wall presence [18]. Confinement-related collective phenomena include spontaneous formation of string-like drop configurations [9, 10], propagation of displacement waves in linear trains of drops in Poiseuille flow [19, 20], instabilities of confined particle jets [21], and pattern formation and rearrangements of particle lattice in 2D regular particle arrays [20]. However, while the above studies revealed rich dynamics resulting from hydrodynamic interactions of particles with the channel walls, a comprehensive understanding of mechanisms underlying the confinement effects is still lacking.

Confinement-induced multiparticle collective phenomena often emerge as a result of hydrodynamic interactions associated with the far-field form of the flow produced by the particles moving in the channel [19–23]. Due to confinement, this flow qualitatively differs from the far-field flow caused by particle motion in free space. The difference stems from the strong fluid-volume conservation constraint associated with the wall presence, and from absorption of momentum by the walls. Owing to the momentum absorption, the velocity field decays too fast to produce a nonzero fluid flux through the boundary at infinity. Therefore, the fluid displaced by a moving particle creates a backflow pattern [4, 22–24] in order to ensure fluid incompressibility. In contrast, in unbounded

systems the fluid in the whole space moves in the same direction as the particle.

The far-field backflow produced by a particle in a channel has a form of a parabolic Hele–Shaw flow driven by a 2D dipolar pressure distribution [4, 22–24]. The Hele–Shaw form of the flow far from the particle can be derived using an appropriate lubrication expansion [25]. The dipolar character of the velocity field around a spherical particle results from the cylindrical symmetry of the problem.

An immediate consequence of the backflow effect is the negative sign of the transverse component of the two-particle mutual hydrodynamic-mobility coefficient [3, 22]. The backflow also causes a large resistance of elongated particles in a narrow channel [3, 4, 7, 23]. Furthermore, collective action of the dipolar flow fields produced by individual particles gives rise to propagation of particle-displacement waves in linear particle arrays in Poiseuille flow [19], and it governs macroscopic deformation and lattice rearrangements in regular particle arrays [20].

The dipolar far-field flow produced by the particles in a channel is crucial not only for understanding suspension dynamics on the particle scale, but also for describing the macroscopic fluid and particle transport. We show that particle contribution to the macroscopic volume flux in suspension flow through the channel can be determined from the amplitudes of the dipolar Hele–Shaw far-field flows produced by the particles. This behavior has a close physical analogy in electrostatics, where the induced electric dipole moments of the molecules of a dielectric material contribute to the electric displacement field. We explore this analogy in our analysis of particle and fluid transport through a channel.

Our paper is organized as follows. Far-field dipolar particle response and particle polarizability are discussed

in Sec. II, where we give a general outline of our theory. The dipole moment of an arbitrary induced-force distribution in a channel is evaluated in Sec. III. The polarizability coefficients for a spherical particle are determined in the friction and mobility formulations in Sec. IV. The results from the preceding sections are used to analyze macroscopic suspension flow in Secs. V and VI: Sec. V relates the macroscopic suspension velocity to the dipolar density per unit area of the channel, and Sec. VI provides macroscopic transport equations describing the particle and fluid transport. Our conclusions are drawn in Sec. VII.

An important additional result of this study is the derivation of explicit Ewald-summation expressions for the periodic Green's functions for Stokes flow in the parallel-wall geometry. These formulations are used in our current numerical simulations to supplement the theoretical analysis, and our expressions are also applicable in Stokesian-dynamics and boundary-integral algorithms for dispersion flows in parallel-wall channels.

II. PARTICLE POLARIZABILITY

In this section we focus on a general discussion of the far-field response of a spherical particle in a parallel-wall channel to an applied lateral force \mathcal{F} , torque \mathcal{T} , and Poiseuille flow \mathbf{v}^{ext} driven by a constant lateral pressure gradient $\nabla_{\parallel} p^{\text{ext}}$. This response is represented in terms of particle polarizability coefficients, which are subsequently used to determine the macroscopic constitutive relations describing suspension transport in a channel.

Our results for the particle response to external forcing can also be used to construct a simplified description of particle dynamics in parallel-wall channels. In this simplified formulation (summarized in Sec. II C 2), the interparticle hydrodynamic interactions are incorporated solely through the far-field flow, in analogy to the point-particle approximation for unbounded systems. As discussed in [20], such a single-scattering approximation yields accurate results if the interparticle separation is sufficiently large.

A. System definition

We consider the dynamics of a spherical particle of radius a (or an array of such particles) in a parallel-wall channel of width H , under creeping-flow conditions. The walls are in the planes $z = 0$ and $z = H$, and the particle center is at the axis z at a distance $z = Z$ from the lower wall. The fluid velocity field satisfies the no-slip boundary conditions on the walls and the particle surface.

For simplicity, the analysis presented in Secs. II–IV is for a single particle in the channel. However, our theoretical formulation can be readily generalized to multi-particle systems. We use such a generalization in Secs.

V and VI, where we consider macroscopic response of suspension to external forcing.

B. Far-field scattered flow

In the near-field regime $\rho \sim H$ (where $\rho = |\boldsymbol{\rho}|$, and $\boldsymbol{\rho} = x\hat{\mathbf{e}}_x + y\hat{\mathbf{e}}_y$ is the lateral position with respect to the particle center) the flow field scattered by the particle, \mathbf{v}' , has a complex 3D form that involves multiple image singularities [26]. However, in the far-field regime ($\rho \gg H$) the scattered flow tends exponentially (on the lengthscale H) to a much simpler 2D Hele–Shaw flow of the form [23]

$$\mathbf{v}'(\mathbf{r}) = -\frac{1}{2}\eta^{-1}z(H-z)\nabla_{\parallel}p'(\boldsymbol{\rho}), \quad (1)$$

where η is the fluid viscosity, p' is the perturbation pressure, ∇_{\parallel} is the gradient operator with respect to the lateral coordinates $\boldsymbol{\rho}$, and $\mathbf{r} = \boldsymbol{\rho} + z\hat{\mathbf{e}}_z$.

Away from the singularity at $\boldsymbol{\rho} = 0$, the pressure field p' satisfies the 2D Laplace equation

$$\nabla_{\parallel}^2 p'(\boldsymbol{\rho}) = 0, \quad \boldsymbol{\rho} \neq 0, \quad (2)$$

owing to the flow incompressibility. For a single particle moving under the action of an external force, torque, or Poiseuille flow, the pressure p' assumes the form of a 2D dipolar field, due to the cylindrical symmetry of the problem and the vectorial character of the forcing. Accordingly, we have

$$p'(\boldsymbol{\rho}) = -\frac{1}{2\pi}\mathbf{D} \cdot \nabla_{\parallel}\Phi_0^-(\boldsymbol{\rho}) = \frac{1}{2\pi}\mathbf{D} \cdot \frac{\boldsymbol{\rho}}{\rho^2}, \quad (3)$$

where

$$\Phi_0^-(\boldsymbol{\rho}) = -\ln(\rho) \quad (4)$$

is the solution of the 2D Poisson equation

$$\nabla_{\parallel}^2 \Phi_0^-(\boldsymbol{\rho}) = -2\pi\delta(\boldsymbol{\rho}), \quad (5)$$

and \mathbf{D} is the dipole moment of the perturbation pressure p' .

As discussed in the introduction, the Hele–Shaw flow (1) with the dipolar pressure distribution (3) involves the backflow effect. Namely, on the symmetry axis parallel to the dipole moment \mathbf{D} , the fluid displaced by the particle is moving in the direction of \mathbf{D} , whereas on the transverse axis it is moving in the opposite direction.

C. Polarizability and mobility relations

Since the dynamics of the system is governed by the linear Stokes equations, the dipole moment \mathbf{D} is linear in the strength of the external forcing,

$$\frac{1}{12}\eta^{-1}H^3\mathbf{D} = \boldsymbol{\mu}^{\text{pt}} \cdot \mathcal{F} + \boldsymbol{\mu}^{\text{pr}} \cdot \mathcal{T} + \boldsymbol{\mu}^{\text{pp}}\nabla_{\parallel}p^{\text{ext}} \quad (6)$$

(where the factor $\frac{1}{12}\eta^{-1}H^3$ is introduced to ensure the Lorentz symmetry for the matrix of transport coefficient, as explained in Sec. IV). The dipolar far-field perturbation pressure (3) is analogous to a 2D electrostatic dipolar potential. Relation (6) will thus be termed a polarizability relation, and the linear transport coefficients μ^{pA} ($A = p, t, r$) will be referred to as the polarizability coefficients (by analogy with an electrostatic problem of polarizable particles in an external electric field).

Apart from producing the far-field response described by Eqs. (1)–(6), a particle in a channel also undergoes translational and rotational motion with the linear and angular velocities \mathbf{U} and $\mathbf{\Omega}$. This rigid-body particle motion is characterized by the standard mobility relations

$$\mathbf{U} = \mu^{tt} \cdot \mathcal{F} + \mu^{tr} \cdot \mathcal{T} - \mu^{tp} \cdot \nabla_{\parallel} p^{\text{ext}}, \quad (7a)$$

$$\mathbf{\Omega} = \mu^{rt} \cdot \mathcal{F} + \mu^{rr} \cdot \mathcal{T} - \mu^{rp} \cdot \nabla_{\parallel} p^{\text{ext}}, \quad (7b)$$

where μ^{AB} denotes hydrodynamic mobility coefficients.

By a partial inversion of equations (6) and (7), the particle response can also be expressed in a friction-relation form, where the velocities \mathbf{U} and $\mathbf{\Omega}$ are the independent variables, and the forces \mathcal{F} and \mathcal{T} are the dependent quantities (cf. Sec. IV).

Equations (6) and (7) are related. Namely, as shown in Sec. IV, the matrix of mobility and polarizability coefficients μ^{AB} satisfies the Lorentz symmetry

$$\mu^{AB} = \mu^{BA\dagger}, \quad A, B = t, r, p, \quad (8)$$

where the dagger denotes the transpose of a tensor [27]. Equation (8) has significant consequences for suspension dynamics in parallel-wall channels, because it implies the corresponding Onsager reciprocal relation for the matrix of kinetic coefficients in the linear constitutive relation describing macroscopic suspension transport.

1. Macroscopic suspension flow

The polarizability relation (6) (and its multiparticle generalization) is essential for theoretical understanding of the macroscopic behavior of suspensions confined in a parallel-wall channel. This relation is also important for numerical evaluation of effective transport coefficients governing the suspension flux.

In the following sections we demonstrate that the average suspension velocity $\bar{\mathbf{u}}$ can be expressed in terms of the average dipole moment of the particles $\bar{\mathbf{D}}$. Specifically, in Sec. V it is shown that

$$\bar{\mathbf{u}} = \kappa_0 (-\nabla_{\parallel} \bar{p} + \bar{n}_s \bar{\mathbf{D}}), \quad (9)$$

where

$$\kappa_0 = \frac{1}{12}\eta^{-1}H^2 \quad (10)$$

is the permeability of a particle-free channel, $\nabla_{\parallel} \bar{p}$ is the macroscopic pressure gradient, and \bar{n}_s is the particle number density per unit area of the channel wall. Equation (9), supplemented with the polarizability relation (6) (averaged over the particle distribution) describes the macroscopic suspension flow (cf. Secs. V and VI).

An intuition regarding physical interpretation of Eq. (9) can be gained by considering its electrostatic analogy. A comparison of the hydrodynamic and electrostatic problems indicates that the macroscopic pressure field is analogous to the electrostatic potential, and the pressure gradient corresponds to the electric field. The macroscopic suspension velocity $\bar{\mathbf{u}}$ (which is divergence free due to the fluid incompressibility) corresponds to the electric-displacement field in the absence of external charges. Relation (9) is thus similar to the expression for the electrostatic displacement field in terms of the electric field and the induced-dipole-moment density [28]. In Sec. V we further explore this analogy.

A macroscopic theory based on the transport equations (6), (7), and (9) is capable of describing complex phenomena that occur in suspension flows in a parallel-wall channels. In particular, we have shown in our recent study [20] that such a theory predicts a fingering instability in evolving 2D particle arrays (which has been confirmed by direct numerical simulations).

2. Single-scattering approximation

The amplitude \mathbf{D} of the dipolar Hele–Shaw flow scattered by a particle in a channel is a key quantity in a single-scattering approximation, where the one-particle polarizability and mobility relations (6) and (7) are combined with an assumption that the incident flow acting on a given particle is a superposition of the external flow and the far-field dipolar flows (1) produced by other particles.

The single-scattering approximation describes particle dynamics in dilute suspensions in parallel-wall channels under the strong-confinement condition $H \sim 2a$. Many fundamental collective phenomena in confined suspension flows (e.g. instabilities of confined particle jets [21], propagation of particle-displacement waves in 1D arrays of drops [19], and pattern formation in 2D regular particle arrays [20]) are driven by the far-field interparticle interactions associated with the dipolar scattered flow (1) and (3). Not only can essential qualitative features of such phenomena be captured using the single-scattering approximation, but it also gives accurate quantitative results if the interparticle distances are sufficiently large [29].

Quantitative predictions using the single-scattering approach require predetermination of the polarizability and mobility coefficients in Eqs. (6) and (7). We evaluate only the polarizability coefficients μ^{pB} ($B = t, r, p$), because the mobility coefficients μ^{AB} ($A = t, r, B = t, r, p$) for spherical particles between two parallel walls have al-

ready been calculated [1–4, 23].

III. DIPOLE MOMENT OF INDUCED-FORCE DISTRIBUTION

To evaluate the induced dipole moment of a particle in a channel, we need to solve the corresponding Stokes-flow problem. For this purpose, we apply the induced-force formulation and multipolar-expansion techniques. In this section we use the asymptotic Liron–Mochon formula for the Green’s function for Stokes flow in the parallel-wall geometry [24], to relate the dipole moment \mathbf{D} to the force distribution induced on the particle. We employ these results in Sec. IV to calculate the polarizability coefficients, and in Secs. V and VI to determine constitutive relations describing macroscopic suspension flow.

A. Induced-force formulation

In our approach, the effect of a particle on the surrounding fluid is represented in terms of the induced-force distribution on the particle surface

$$\mathbf{F}(\mathbf{r}) = a^{-2}\delta(r_1 - a)\mathbf{f}_1(\mathbf{r}_1), \quad (11)$$

where $\mathbf{r}_1 = \mathbf{r} - Z\hat{\mathbf{e}}_z$ denotes the position with respect to the particle center, and $r_1 = |\mathbf{r}_1|$. By definition of the induced force, the flow and pressure fields produced by the distribution (11) are identical to the velocity field $\mathbf{v}(\mathbf{r})$ and pressure $p(\mathbf{r})$ in the particle presence [30–32].

For a particle in an external flow $\mathbf{v}^{\text{ext}}(\mathbf{r})$, the velocity and pressure fields can be represented by the boundary integrals

$$\mathbf{v}(\mathbf{r}) = \mathbf{v}^{\text{ext}}(\mathbf{r}) + \int \mathbf{T}(\mathbf{r}, \mathbf{r}') \cdot \mathbf{F}(\mathbf{r}') d\mathbf{r}', \quad (12a)$$

$$p(\mathbf{r}) = p^{\text{ext}}(\mathbf{r}) + \int \mathbf{Q}(\mathbf{r}, \mathbf{r}') \cdot \mathbf{F}(\mathbf{r}') d\mathbf{r}', \quad (12b)$$

where $p^{\text{ext}}(\mathbf{r})$ is the external pressure associated with the flow $\mathbf{v}^{\text{ext}}(\mathbf{r})$, and \mathbf{T} and \mathbf{Q} are the velocity and pressure Green’s functions for a parallel-wall channel.

The Green’s functions for Stokes flow in the parallel-wall geometry were investigated using several different methods [1–4, 23, 24, 26]. In the Cartesian-representation approach proposed by our group [3, 4, 23], the velocity and pressure Green’s functions $\mathbf{T}(\mathbf{r}, \mathbf{r}')$ and $\mathbf{Q}(\mathbf{r}, \mathbf{r}')$ are represented in terms of lateral Fourier integrals of simple matrix products. The explicit formulas are listed in Appendix A.

For a particle moving with the translational and angular velocities \mathbf{U} and $\mathbf{\Omega}$, the flow field (12a), evaluated at the particle surface S , equals the rigid body velocity of the particle

$$\mathbf{v}(\mathbf{r}) = \mathbf{v}^{\text{rb}}(\mathbf{r}) \equiv \mathbf{U} + \mathbf{\Omega} \times \mathbf{r}_1, \quad \mathbf{r} \in S. \quad (13)$$

With the above boundary condition, Eq. (12a) yields a boundary-integral equation for the induced forces.

For a given induced-force distribution (11) the force and torque acting on the particle can be evaluated using expressions

$$\mathcal{F} = \int \mathbf{F}(\mathbf{r}) d\mathbf{r}, \quad \mathcal{T} = \int \mathbf{r} \times \mathbf{F}(\mathbf{r}) d\mathbf{r}. \quad (14)$$

In the following section we determine the corresponding relation for the amplitude of the dipolar far-field flow produced by the particle.

B. Dipole moment

The dipolar strength \mathbf{D} of a force distribution \mathbf{F} can be obtained from Eqs. (12) using asymptotic far-field expressions for the Green’s function \mathbf{T} and \mathbf{Q} . (Such expressions were first derived by Liron and Mochon [24]; an alternative and much simpler derivation via a lubrication expansion is given in [25]).

As discussed in [23], the asymptotic form of the flow and pressure Green’s functions, $\mathbf{T}_{\text{HS}}(\mathbf{r}, \mathbf{r}')$ and $\mathbf{Q}_{\text{HS}}(\mathbf{r}, \mathbf{r}')$, can be represented by the following formulas

$$\mathbf{T}_{\text{HS}}(\mathbf{r}, \mathbf{r}') = -\frac{1}{2}\eta^{-1}z(H-z)\nabla\mathbf{Q}_{\text{HS}}(\mathbf{r}, \mathbf{r}'), \quad (15a)$$

$$\mathbf{Q}_{\text{HS}}(\mathbf{r}, \mathbf{r}') = -3\pi^{-1}H^{-3}\nabla\Phi_0^-(\boldsymbol{\rho} - \boldsymbol{\rho}')z'(H-z'), \quad (15b)$$

where $\boldsymbol{\rho} = x\hat{\mathbf{e}}_x + y\hat{\mathbf{e}}_y$ and $\boldsymbol{\rho}' = x'\hat{\mathbf{e}}_x + y'\hat{\mathbf{e}}_y$ are the lateral position vectors, and $\Phi_0^-(\boldsymbol{\rho})$ is the point-source solution (4) of the 2D Poisson equation (5). We note that the asymptotic Hele–Shaw flow and pressure fields (15) satisfy the Stokes equations exactly. However, these fields have a different singularity than the original point-force singularity of the full Green’s functions \mathbf{T} and \mathbf{Q} .

According to Eqs. (15b) and (4), the far-field pressure

$$p^{\text{d}}(\boldsymbol{\rho}) = \mathbf{Q}_{\text{HS}}(\mathbf{r}, \mathbf{r}') \cdot \mathbf{F}_{\parallel} \quad (16)$$

produced by a lateral point force \mathbf{F}_{\parallel} has a form of a 2D potential dipole

$$p^{\text{d}}(\boldsymbol{\rho}) = -\frac{1}{2\pi}\mathbf{D}_0 \cdot \nabla_{\parallel}\Phi_0^-(\boldsymbol{\rho} - \boldsymbol{\rho}') \quad (17)$$

with the dipole moment

$$\mathbf{D}_0 = 6H^{-3}z'(H-z')\mathbf{F}_{\parallel}. \quad (18)$$

The streamlines of the corresponding velocity field

$$\mathbf{v}^{\text{d}}(\mathbf{r}) = -\frac{1}{2}\eta^{-1}z(H-z)\nabla_{\parallel}p^{\text{d}}(\boldsymbol{\rho}) \quad (19)$$

also follow a 2D dipolar pattern. The quadratic dependence of the dipolar strength (18) on the position z' of the point where the force is applied follows from the Lorentz’s symmetry of the Green’s function (15a) [23]. We note

that the flow field produced by a transverse force (i.e. a force pointing in the z direction) is exponentially small in the far-field domain.

Similar to the corresponding electrostatic problem, the dipole moment (18) represents not only the amplitude of the far-field pressure (16) but also the strength of the dipolar-pressure source,

$$\nabla_{\parallel}^2 p^d(\boldsymbol{\rho}) = \mathbf{D}_0 \cdot \nabla_{\parallel} \delta(\boldsymbol{\rho} - \boldsymbol{\rho}'). \quad (20)$$

In Sec. V the above expression will be used in our derivation of the relation between the macroscopic dipolar-strength density per unit area of the channel and the average suspension flow.

The dipole moment of the far-field perturbation pressure (3) produced by a particle in a channel is evaluated by integrating (18) over the particle surface. Taking $\mathbf{F}_{\parallel} = l_{\parallel} \mathbf{F}(\mathbf{r})$, where

$$l_{\parallel} = \hat{\mathbf{e}}_x \hat{\mathbf{e}}_x + \hat{\mathbf{e}}_y \hat{\mathbf{e}}_y \quad (21)$$

denotes the projection operator onto the lateral directions x and y , and $\mathbf{F}(\mathbf{r})$ is the induced-force distribution (11), we get

$$\mathbf{D} = 6H^{-3} \int z'(H - z') l_{\parallel} \cdot \mathbf{F}(\mathbf{r}') d\mathbf{r}'. \quad (22)$$

In the following section, Eq. (22) is used to determine the polarizability coefficients of a particle.

IV. POLARIZABILITY COEFFICIENTS

A. Multipolar expansion

To determine the force distribution induced on the particle surface, the boundary-value problem (12a) and (13) is solved using the multipolar-expansion technique [3, 4, 23]. In our method, the induced-force distribution and the flow field in the system are expanded into the conjugate sets of basis functions introduced in [33]. In particular, we have the expansions

$$\mathbf{F}(\mathbf{r}) = \sum_{lm\sigma} f(lm\sigma) \mathbf{w}_{lm\sigma}^+(\mathbf{r}_1), \quad (23a)$$

$$\mathbf{v}^{\text{rb}}(\mathbf{r}) - \mathbf{v}^{\text{ext}}(\mathbf{r}) = \sum_{lm\sigma} c(lm\sigma) \mathbf{v}_{lm\sigma}^+(\mathbf{r}_1), \quad (23b)$$

where the left-hand side of Eq. (23b) describes the external flow with respect to the rigid-body particle motion (13).

In the above relations $\mathbf{w}_{lm\sigma}^+$ and $\mathbf{v}_{lm\sigma}^+$ are the conjugate spherical basis functions associated with the non-singular solutions of Stokes equations in spherical coordinates [3, 4, 33], and $f(lm\sigma)$ and $c(lm\sigma)$ are the corresponding expansion coefficients [34]. The flow \mathbf{v}' scattered by the particle has a similar expansion in terms of singular basis

functions $\mathbf{v}_{lm\sigma}^-$. Here $l = 1, 2, \dots$ and $m = 0, \pm 1, \dots, \pm l$ are the spherical harmonic orders of the basis functions, and the index $\sigma = 0, 1, 2$ corresponds to the three types of Lamb's solutions for Stokes flow.

By inserting expansions (23) into relation (12a) evaluated at the particle surface one gets a linear algebraic equation of the form [3, 4]

$$\sum_{l'm'\sigma'} G(lm\sigma | l'm'\sigma') f(l'm'\sigma') = c(lm\sigma), \quad (24)$$

where the matrix elements $G(lm\sigma | l'm'\sigma')$ are defined in terms of the multipolar projections of the Green's function \mathbf{T} ,

$$G(lm\sigma | l'm'\sigma') = \langle \mathbf{w}_{lm\sigma}^+(\mathbf{r}_1) | \mathbf{T} | \mathbf{w}_{l'm'\sigma'}^+(\mathbf{r}_1) \rangle. \quad (25)$$

In Eq. (25) we use the Dirac's bra-ket notation [35]

$$\langle \mathbf{A} | \mathbf{B} \rangle = \int \mathbf{A}^*(\mathbf{r}) \cdot \mathbf{B}(\mathbf{r}) d\mathbf{r}, \quad (26)$$

with the asterisk denoting the complex conjugate.

Equation (25) is valid for a particle with the no-slip boundary conditions on its surface. For other boundary conditions (e.g., spherical viscous drops) the diagonal elements of (25) need to be modified to include an appropriate single-particle scattering matrix [3, 4, 23]. It should also be noted that equation (24) is given here for a single particle, but general expressions for a multiparticle system are readily available [3, 4, 23].

B. Generalized friction matrix

The response of the system to a given rigid-body particle motion (13) and external parabolic flow

$$\mathbf{v}^{\text{ext}} = -\frac{1}{2}\eta^{-1}z(H - z)\nabla p^{\text{ext}} \quad (27)$$

driven by a constant lateral pressure gradient ∇p^{ext} can be characterized by the generalized resistance relation

$$\begin{bmatrix} \mathcal{F} \\ \mathcal{T} \\ \frac{1}{12}H^3\mathbf{D} \end{bmatrix} = \begin{bmatrix} \zeta^{\text{tt}} & \zeta^{\text{tr}} & \zeta^{\text{tp}} \\ \zeta^{\text{rt}} & \zeta^{\text{rr}} & \zeta^{\text{rp}} \\ \zeta^{\text{pt}} & \zeta^{\text{pr}} & \zeta^{\text{pp}} \end{bmatrix} \cdot \begin{bmatrix} \mathbf{U} \\ \boldsymbol{\Omega} \\ \eta^{-1}\nabla p^{\text{ext}} \end{bmatrix}. \quad (28)$$

As discussed below, the factor $\frac{1}{12}H^3$ that multiplies the dipole moment \mathbf{D} is needed to ensure the Lorentz symmetry (35) of the resistance matrix ζ . The coefficients in the bottom row of the matrix ζ characterize the particle polarizability.

The generalized resistance tensors ζ^{AB} can be determined by solving Eq. (24) to evaluate the induced-force amplitudes $f(lm\sigma)$ in terms of the flow expansion coefficients $c(lm\sigma)$. The solution can be represented by the matrix relation

$$f(lm\sigma) = \sum_{l'm'\sigma'} F(lm\sigma | l'm'\sigma') c(l'm'\sigma'), \quad (29)$$

where $F(lm\sigma | l'm'\sigma')$ denotes the elements of the matrix inverse to the Green's matrix $G(lm\sigma | l'm'\sigma')$.

To obtain the resistance formula (28), Eq. (29) has to be supplemented with appropriate expressions that relate the force \mathcal{F} , torque \mathcal{T} , and dipole moment \mathbf{D} to the expansion coefficients $f(lm\sigma)$ of the induced force distribution (23a). We also need the relations for the expansion coefficients $c(lm\sigma)$ associated with a given rigid-body particle motion (13) and external flow (27). These relations can be expressed in terms of the transformation vectors \mathbf{X} , discussed in Appendix B. Namely, we have

$$\mathcal{F} = \sum_{lm\sigma} \mathbf{X}(\mathbf{t} | lm\sigma) f(lm\sigma), \quad (30a)$$

$$\mathcal{T} = \sum_{lm\sigma} \mathbf{X}(\mathbf{r} | lm\sigma) f(lm\sigma), \quad (30b)$$

$$\frac{1}{12} H^3 \mathbf{D} = \sum_{lm\sigma} \mathbf{X}(\mathbf{p} | lm\sigma) f(lm\sigma), \quad (30c)$$

and

$$c(lm\sigma) = \mathbf{X}(lm\sigma | \mathbf{t}) \cdot \mathbf{U} + \mathbf{X}(lm\sigma | \mathbf{r}) \cdot \boldsymbol{\Omega} + \mathbf{X}(lm\sigma | \mathbf{p}) \cdot \eta^{-1} \nabla p^{\text{ext}}, \quad (31)$$

where the transformation vectors \mathbf{X} satisfy the symmetry relation

$$\mathbf{X}(lm\sigma | A) = \mathbf{X}^*(A | lm\sigma). \quad (32)$$

Explicit expressions for the transformation vectors (32) are listed in Appendix B. We note that only several matrix elements with small values of the indices l, m, σ are nonzero, according to Eqs. (B1) and (B2).

Combining Eqs. (29)–(31) yields the relation

$$\zeta^{AB} = \sum_{lm\sigma} \sum_{l'm'\sigma'} \mathbf{X}(A | lm\sigma) F(lm\sigma | l'm'\sigma') \mathbf{X}(l'm'\sigma' | B), \quad A, B = \mathbf{t}, \mathbf{r}, \mathbf{p}, \quad (33)$$

for the translational, rotational, and polarizability components of the generalized friction matrix. Taking into account relation (32) and the Lorentz symmetry of the matrix F [3, 4],

$$F(lm\sigma | l'm'\sigma') = F^*(l'm'\sigma' | lm\sigma), \quad (34)$$

we obtain the corresponding symmetry of the generalized friction matrix

$$\zeta^{AB} = \zeta^{BA\dagger}. \quad (35)$$

The symmetry relation (35) with $A, B = \mathbf{t}, \mathbf{r}$ corresponds to the well-known Lorentz symmetry of the standard resistance matrix [36]. For $A = \mathbf{p}$ or $B = \mathbf{p}$, however, the symmetry relation (35) is new, and its importance becomes clear in Sec. V, where we explain the relationship between the dipole moment induced on the particles and the macroscopic suspension flow.

C. Mobility formulation

The polarizability and mobility relations (6) and (7) can be obtained by partially inverting the generalized resistance relation (28). In the matrix representation anal-

ogous to (28) we have

$$\begin{bmatrix} \mathbf{U} \\ \boldsymbol{\Omega} \\ \frac{1}{12} \eta^{-1} H^3 \mathbf{D} \end{bmatrix} = \begin{bmatrix} \boldsymbol{\mu}^{\text{tt}} & \boldsymbol{\mu}^{\text{tr}} & \boldsymbol{\mu}^{\text{tp}} \\ \boldsymbol{\mu}^{\text{rt}} & \boldsymbol{\mu}^{\text{rr}} & \boldsymbol{\mu}^{\text{rp}} \\ \boldsymbol{\mu}^{\text{pt}} & \boldsymbol{\mu}^{\text{pr}} & -\boldsymbol{\mu}^{\text{pp}} \end{bmatrix} \cdot \begin{bmatrix} \mathcal{F} \\ \mathcal{T} \\ -\nabla p^{\text{ext}} \end{bmatrix}, \quad (36)$$

where

$$\begin{bmatrix} \boldsymbol{\mu}^{\text{tt}} & \boldsymbol{\mu}^{\text{tr}} \\ \boldsymbol{\mu}^{\text{rt}} & \boldsymbol{\mu}^{\text{rr}} \end{bmatrix} = \begin{bmatrix} \zeta^{\text{tt}} & \zeta^{\text{tr}} \\ \zeta^{\text{rt}} & \zeta^{\text{rr}} \end{bmatrix}^{-1}, \quad (37)$$

$$\eta \begin{bmatrix} \boldsymbol{\mu}^{\text{tp}} \\ \boldsymbol{\mu}^{\text{rp}} \end{bmatrix} = \begin{bmatrix} \zeta^{\text{tt}} & \zeta^{\text{tr}} \\ \zeta^{\text{rt}} & \zeta^{\text{rr}} \end{bmatrix}^{-1} \cdot \begin{bmatrix} \zeta^{\text{tp}} \\ \zeta^{\text{rp}} \end{bmatrix}, \quad (38)$$

$$\begin{bmatrix} \boldsymbol{\mu}^{\text{pt}} & \boldsymbol{\mu}^{\text{pr}} \end{bmatrix} = \begin{bmatrix} \boldsymbol{\mu}^{\text{tp}} \\ \boldsymbol{\mu}^{\text{rp}} \end{bmatrix}^\dagger, \quad (39)$$

$$\eta^2 \boldsymbol{\mu}^{\text{pp}} = \zeta^{\text{pp}} - \begin{bmatrix} \zeta^{\text{pt}} & \zeta^{\text{pr}} \end{bmatrix} \cdot \begin{bmatrix} \zeta^{\text{tt}} & \zeta^{\text{tr}} \\ \zeta^{\text{rt}} & \zeta^{\text{rr}} \end{bmatrix}^{-1} \cdot \begin{bmatrix} \zeta^{\text{tp}} \\ \zeta^{\text{rp}} \end{bmatrix}. \quad (40)$$

Similar to the corresponding property of the friction matrix, the generalized mobility matrix $\boldsymbol{\mu}^{AB}$ satisfies the Lorentz symmetry (8), which is obtained by combining (35) with (37)–(40). Note that the negative sign is incorporated into the pressure-gradient term on the right-hand side of Eq. (36) to obtain positive signs of the “pt” and

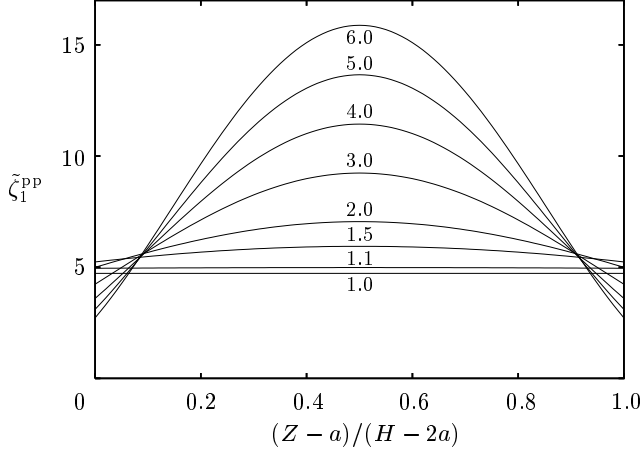


FIG. 1: Normalized polarizability coefficient (43), versus particle position scaled by the vertical space available in the channel, for channel width $H/(2a)$ (as labeled). Coefficient $\tilde{\zeta}_1^{pp}$ characterizes the amplitude of the far-field flow produced by an immobile particle in an external pressure-driven flow.

“pr” components of the matrix $\boldsymbol{\mu}$. We have also included factors η and η^2 in Eqs. (38) and (40), to ensure that the polarizability and mobility coefficients have appropriate dimensionalities.

The generalized mobility and friction tensors (28) and (36) are given here only for a single sphere. However, their multiparticle generalizations can easily be obtained.

D. Tensorial form

For a single spherical particle, considered herein, the friction and mobility tensors $\boldsymbol{\psi}^{AB} = \boldsymbol{\zeta}^{AB}$, $\boldsymbol{\mu}^{AB}$ are invariant with respect to rotation around the axis z . Noting that $\boldsymbol{\mathcal{T}}$ and $\boldsymbol{\Omega}$ are pseudo-vectors, and that ∇p^{ext} has only lateral components we find that

$$\psi^{AA} = \psi^{AA} \mathbf{I}_{\parallel} + \psi_{\perp}^{AA} \hat{\mathbf{e}}_z \hat{\mathbf{e}}_z, \quad A = t, r, \quad (41a)$$

$$\psi^{AB} = \psi^{AB} \mathbf{I}_{\parallel}, \quad A = p, \quad B = t, p, \quad (41b)$$

$$\psi^{AB} = \psi^{AB} \boldsymbol{\epsilon}_{\parallel}, \quad A = t, p, \quad B = r, \quad (41c)$$

where \mathbf{I}_{\parallel} is the lateral unit tensor (21), and

$$\boldsymbol{\epsilon}_{\parallel} = \hat{\mathbf{e}}_x \hat{\mathbf{e}}_y - \hat{\mathbf{e}}_y \hat{\mathbf{e}}_x \quad (42)$$

is the lateral alternating tensor. The remaining components of the tensors $\boldsymbol{\psi}^{AB}$ are obtained using the reciprocal relations (8) and (35). In Eqs. (41), the lateral transport coefficients are denoted by ψ^{AB} , and the transverse coefficients by ψ_{\perp}^{AB} .

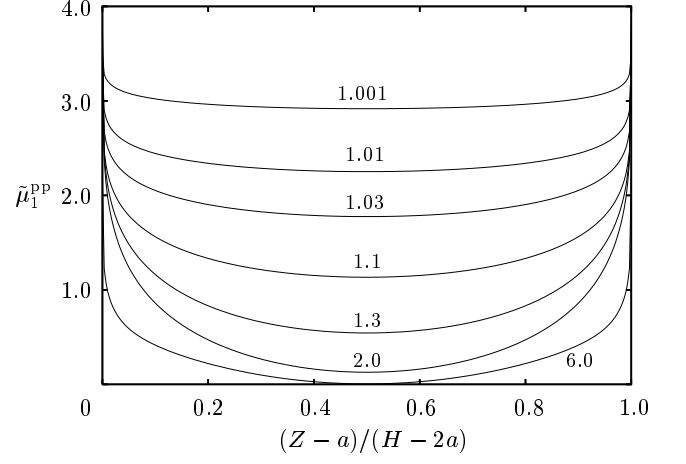


FIG. 2: Normalized polarizability coefficient (45), versus particle position scaled by the vertical space available in the channel, for channel width $H/(2a)$ (as labeled). Coefficient $\tilde{\mu}_1^{pp}$ characterizes the amplitude of the far-field flow produced by a freely moving particle in an external pressure-driven flow.

E. Numerical results

In this section we present our numerical results for the generalized resistance and mobility matrices $\boldsymbol{\zeta}$ and $\boldsymbol{\mu}$. Since we are concerned here with the effect of the far-field flow on the system dynamics, we focus on the polarizability components that relate the external forcing to the induced dipole moment of the particle.

We note that the translational and rotational components of the friction and mobility matrices were calculated by Jones [2] and by our group [3, 4]. The effect of an external Poiseuille flow on particle motion has also been determined [1, 2, 23]. The polarizability coefficients ψ^{pt} and ψ^{pr} ($\psi = \zeta, \mu$) can be calculated from these earlier results by invoking the Lorentz symmetries (8) and (35). The coefficient ψ^{pp} , introduced here, has never been considered.

1. Immobile particle

The dependence of the polarizability coefficient ζ^{pp} on the channel width and the transverse particle position Z is depicted in Fig. 1. The results are presented for the normalized coefficient

$$\tilde{\zeta}_1^{\text{pp}} = \frac{12\zeta^{\text{pp}}}{\pi\eta H^3 a^2}, \quad (43)$$

where the subscript 1 indicates that the quantity (43) is evaluated for an isolated particle in the channel. According to equation (28), the coefficient (43) represents the dimensionless dipole moment

$$\tilde{D} = \frac{|\mathbf{D}|}{\pi a^2 |\nabla p^{\text{ext}}|} \quad (44)$$

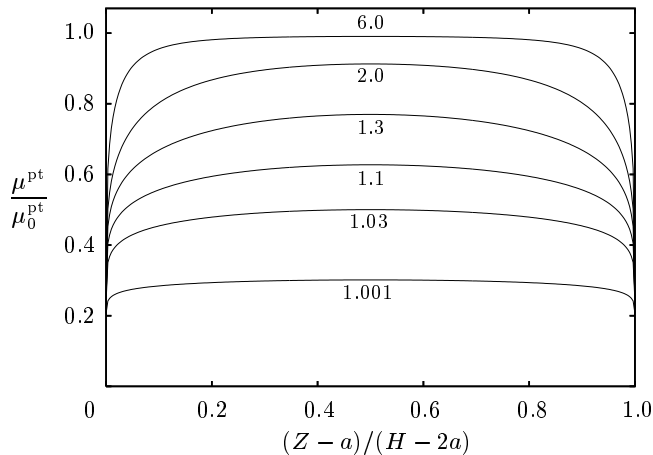


FIG. 3: Translational polarizability coefficient μ^{pt} , normalized by the corresponding result for the point force (47), versus particle position scaled by the vertical space available in the channel, for channel width $H/(2a)$ (as labeled). Coefficient μ^{pt} characterizes the amplitude of the far-field flow produced by a particle moving under the action of a lateral force.

produced by the imposed pressure gradient ∇p^{ext} . As discussed in Sec. VIA, the normalized polarizability coefficient $\tilde{\zeta}_1^{\text{pp}}$ appears as the leading-order term in the volume-fraction expansion of the permeability of a fixed bed of particles in the channel. The normalization has been chosen to simplify the resulting expression.

The results in Fig. 1 indicate that the induced dipole moment (44) has a pronounced maximum for a particle in the midplane of the channel, especially for larger values of the channel width H . This behavior results from two factors: First, the flow acting on an immobile particle is the strongest in the center of the channel; and second, the induced force applied at point z' produces the strongest far-field flow for $z' = H/2$, according to Eq. (18).

2. Suspended particle

For a freely moving suspended particle, the numerical results are shown for three polarizability coefficients: μ^{pp} , μ^{pt} , and μ^{pr} . These coefficients characterize the induced dipole moment produced by the external flow, force and torque acting on the suspended particle.

Figure 2 illustrates the dependence of the polarizability coefficient μ^{pp} on the channel width and the particle position. The normalization of the results is analogous to the normalization used in Fig. 1 for ζ^{pp} ,

$$\tilde{\mu}_1^{\text{pp}} = \frac{12\eta\mu^{\text{pp}}}{\pi H^3 a^2}, \quad (45)$$

except that the viscosity appears in the numerator, because of the factor η in the definition (40) of μ^{pp} . The normalized polarizability coefficient (45) is equivalent to the dimensionless dipole moment (44) produced by the

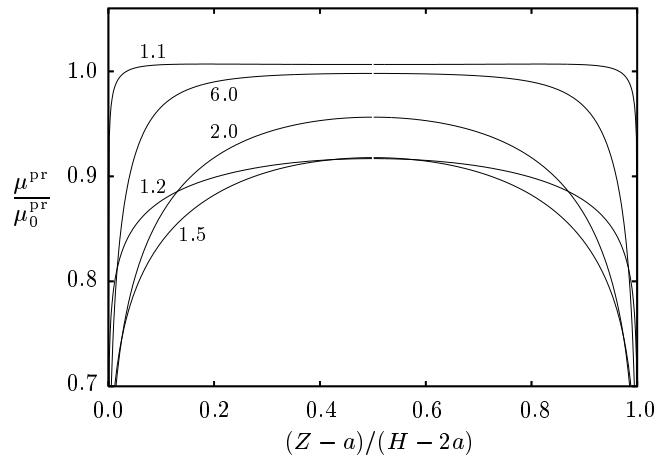


FIG. 4: Translational polarizability coefficient μ^{pr} , normalized by the corresponding result for the point torque (48), versus particle position scaled by the vertical space available in the channel, for channel width $H/(2a)$ (as labeled). Coefficient μ^{pr} characterizes the amplitude of the far-field flow produced by a particle moving under the action of a lateral torque.

pressure gradient ∇p^{ext} acting on a force- and torque-free particle.

A comparison of the results shown in Fig. 2 with those depicted in Fig. 1 indicates that

$$\tilde{\mu}_1^{\text{pp}} \leq \tilde{\zeta}_1^{\text{pp}}, \quad (46)$$

where the equal sign holds for a particle touching the wall. In such configurations the particle cannot move, owing to the diverging lubrication forces. Thus the particle polarizability is the same in the mobility and friction formulations. Relation (46) is consistent with a general observation that the energy dissipation is larger in a system with more constraints, which can be demonstrated using variational techniques [37]. Relation (46) can also be directly obtained from (40), by observing that the translation-rotation resistance matrix is positive definite.

The results shown in Fig. 2 indicate that $\tilde{\mu}_1^{\text{pp}}$ has a minimum at $Z = H/2$, and that for large values of $H/(2a)$ the minimal value nearly vanishes. This is because for force- and torque-free particle and large wall separation, the dominant contribution to the dipole moment \mathbf{D} comes from the stresslet induced on the particle due to the local velocity gradient of the imposed parabolic flow. At the center of the channel, the imposed velocity gradient vanishes, so there is no stresslet contribution.

Our results for the translational and rotational polarizability coefficients μ^{pt} and μ^{pr} are shown in Figs. 3 and 4. To emphasize the effect of the particle size and position on the dipole moment \mathbf{D} , the translational polarizability is normalized by the coefficient

$$\mu_0^{\text{pt}}(Z) = \frac{1}{2}\eta^{-1}Z(H - Z), \quad (47)$$

corresponding to the dipole moment (18) of a unit lateral point force (Stokeslet) applied to the fluid at the position

Z . Similarly, the rotational polarizability is normalized by the coefficient

$$\mu_0^{\text{pr}}(Z) = \frac{1}{2}\eta^{-1}(\frac{1}{2}H - Z), \quad (48)$$

representing the dipole moment associated with the dipolar far-field flow produced by a unit lateral point torque (rotlet) [23, 25, 38]. Note that (47) is symmetric and (48) is antisymmetric with respect to the channel center.

The results in Figs. 3 and 4 indicate that $\mu^{\text{pt}}/\mu_0^{\text{pt}} \approx \mu^{\text{pr}}/\mu_0^{\text{pr}} \approx 1$ for $H/(2a) \gg 1$, except for the regions adjacent to the walls, where the normalized polarizabilities decrease logarithmically to zero for a particle touching a wall. The normalized polarizability $\mu^{\text{pt}}/\mu_0^{\text{pt}}$ decreases monotonically with decreasing wall separation, whereas $\mu^{\text{pr}}/\mu_0^{\text{pr}}$ is non-monotonic in $H/(2a)$.

V. MACROSCOPIC SUSPENSION FLOW

In this section we apply the results of the above analysis to determine the average volume flux in a dilute suspension bounded by two parallel planar walls. The average flow can be driven by the macroscopic pressure gradient, by lateral forces or by lateral torques applied to the particles.

To determine macroscopic equations governing suspension flow, we first show that the far-field Hele–Shaw flow (1) driven by the dipolar pressure distribution (3) contributes to the macroscopic suspension velocity. This behavior is analogous to the 2D electrostatics, where the electric field produced by induced dipoles contributes to the macroscopic electrostatic displacement field (as discussed in Sec. II C 1).

The electrostatic analogy can be directly applied to fluid flow through a system of immobile particles in a channel. In this case the fluid transport is governed by the Darcy’s equation

$$\bar{\mathbf{u}} = -\kappa \nabla_{\parallel} \bar{p}, \quad (49)$$

which is a counterpart of the constitutive relation between the electric and electrostatic-displacement fields. In equation (49) $\nabla_{\parallel} \bar{p}$ denotes the macroscopic pressure gradient, and $\bar{\mathbf{u}}$ is the macroscopic velocity, defined as fluid-flux density averaged across the channel. The effective permeability coefficient κ plays a role similar to that of the effective dielectric constant in the corresponding electrostatic system. Equation (49) can be obtained by combining Eq. (9) with the “pp” component of Eq. (28).

Note that relations (9) and (49) involve the macroscopic pressure gradient (rather than the gradient of the external pressure p^{ext}), to ensure that the constitutive relations involve only local quantities and are independent of the boundary conditions.

For a system of particles suspended in a fluid, suspension transport is described by a constitutive equation that includes additional force and torque contributions,

$$H\bar{\mathbf{u}} = \nu^{\text{pt}} \cdot \mathcal{F} + \nu^{\text{pr}} \cdot \mathcal{T} - \nu^{\text{pp}} \nabla_{\parallel} \bar{p}, \quad (50)$$

where ν^{pp} , ν^{pt} , and ν^{pr} are the effective mobility coefficients.

To derive Eq. (9) and determine the transport coefficients in Eqs. (49) and (50), we consider the average pressure gradient and average velocity in a periodic system representing a macroscopically uniform quasi-two-dimensional medium.

A. Periodic Green’s function

We start our analysis by deriving appropriate expressions for the periodic Green’s functions for Stokes flow in a parallel-wall channel. In the present paper, our formulation is used as a theoretical tool to obtain the relation between the quantities $\bar{\mathbf{D}}$ and $\bar{\mathbf{u}}$. Our explicit results are also applied in numerical calculations presented in Sec. VI. More generally, our formulas for the periodic Green’s functions can be employed in Stokesian-dynamics and boundary-integral algorithms for parallel-wall geometry.

1. Near-field and far-field contributions

In our approach, the periodic flow and pressure Green’s functions \mathbf{T}^{per} and \mathbf{Q}^{per} are evaluated by splitting them into the asymptotic Hele–Shaw parts $\mathbf{T}_{\text{HS}}^{\text{per}}$ and $\mathbf{Q}_{\text{HS}}^{\text{per}}$, and quickly convergent lattice sums of 3D corrections to the asymptotic Hele–Shaw behavior,

$$\mathbf{T}^{\text{per}}(\mathbf{r}, \mathbf{r}') = \mathbf{T}_{\text{HS}}^{\text{per}}(\mathbf{r}, \mathbf{r}') + \sum_{\mathbf{n}} \delta \mathbf{T}(\mathbf{r}, \mathbf{r}'_{\mathbf{n}}), \quad (51a)$$

$$\mathbf{Q}^{\text{per}}(\mathbf{r}, \mathbf{r}') = \mathbf{Q}_{\text{HS}}^{\text{per}}(\mathbf{r}, \mathbf{r}') + \sum_{\mathbf{n}} \delta \mathbf{Q}(\mathbf{r}, \mathbf{r}'_{\mathbf{n}}). \quad (51b)$$

Here $\mathbf{n} = (n_x, n_y)$ (with $n_x, n_y = 0, \pm 1 \dots$) are the indices of the periodic lattice,

$$\mathbf{r}'_{\mathbf{n}} = \mathbf{r}' + n_x L_x \hat{\mathbf{e}}_x + n_y L_y \hat{\mathbf{e}}_y \quad (52)$$

are the positions of the periodic images of the source point \mathbf{r}' , and L_x and L_y are the lattice constants. The near-field contributions $\delta \mathbf{T}$ and $\delta \mathbf{Q}$ are defined as the differences between the exact and asymptotic non-periodic Green’s functions,

$$\delta \mathbf{T}(\mathbf{r}, \mathbf{r}') = \mathbf{T}(\mathbf{r}, \mathbf{r}') - \mathbf{T}_{\text{HS}}(\mathbf{r}, \mathbf{r}'), \quad (53a)$$

$$\delta \mathbf{Q}(\mathbf{r}, \mathbf{r}') = \mathbf{Q}(\mathbf{r}, \mathbf{r}') - \mathbf{Q}_{\text{HS}}(\mathbf{r}, \mathbf{r}'). \quad (53b)$$

Since the flow and pressure fields in a parallel-wall channel tend to the asymptotic Hele–Shaw form exponentially on the lengthscale H [23, 24], the near-field contributions (53) exponentially vanish at large lateral distances $\delta \rho$ between the field and source points \mathbf{r} and \mathbf{r}' . Our numerical tests [23] indicate that the exact and asymptotic Green’s functions are nearly identical for $\delta \rho/H \gtrsim 3$. Therefore,

in practical calculations only a small number of terms need to be evaluated to determine the lattice sums in Eqs. (51) with high accuracy.

We note that explicit expressions for all terms in Eqs. (53) are known [cf. Eq. (15) and the results in Appendix A]. Analytic formulas for the asymptotic Hele–Shaw Green’s functions $\mathbf{T}_{\text{HS}}^{\text{per}}$ and $\mathbf{Q}_{\text{HS}}^{\text{per}}$ are derived in the following section and in Appendix C.

2. Far-field Green’s functions for periodic system

To evaluate the far-field components $\mathbf{T}_{\text{HS}}^{\text{per}}$ and $\mathbf{Q}_{\text{HS}}^{\text{per}}$ of the periodic Green’s functions (51) we start from the direct lattice sums

$$\mathbf{T}_{\text{HS}}^{\text{per}}(\mathbf{r}, \mathbf{r}') = \sum_{\mathbf{n}} \mathbf{T}_{\text{HS}}(\mathbf{r}, \mathbf{r}'_{\mathbf{n}}), \quad (54a)$$

$$\mathbf{Q}_{\text{HS}}^{\text{per}}(\mathbf{r}, \mathbf{r}') = \sum_{\mathbf{n}} \mathbf{Q}_{\text{HS}}(\mathbf{r}, \mathbf{r}'_{\mathbf{n}}). \quad (54b)$$

Combining relations (54) with (15) allows us to express the hydrodynamic periodic Green’s functions in the Hele–Shaw regime in terms of the periodic solution of the corresponding electrostatic problem. Accordingly, we have

$$\mathbf{T}_{\text{HS}}^{\text{per}}(\mathbf{r}, \mathbf{r}') = -\frac{1}{2}\eta^{-1}z(H-z)\nabla\mathbf{Q}_{\text{HS}}^{\text{per}}(\mathbf{r}, \mathbf{r}'), \quad (55a)$$

$$\mathbf{Q}_{\text{HS}}^{\text{per}}(\mathbf{r}, \mathbf{r}') = -3\pi^{-1}H^{-3}\nabla w(\boldsymbol{\rho} - \boldsymbol{\rho}')z'(H-z'), \quad (55b)$$

where the Wigner potential $w(\boldsymbol{\rho} - \boldsymbol{\rho}')$, is the periodic solution of the Poisson equation

$$\nabla^2 w(\boldsymbol{\rho} - \boldsymbol{\rho}') = -2\pi \left[\sum_{\mathbf{n}} \delta(\boldsymbol{\rho} - \boldsymbol{\rho}'_{\mathbf{n}}) - S_{\text{p}}^{-1} \right]. \quad (56)$$

Here $\boldsymbol{\rho}'_{\mathbf{n}}$ is the lateral component of the lattice vector (52), and $S_{\text{p}} = L_x L_y$ is the area of a unit cell [39].

The Wigner potential $w(\boldsymbol{\rho} - \boldsymbol{\rho}')$ can be determined using standard Ewald summation techniques [40, 41]. Well-developed accelerated algorithms for calculating this function are also available [40]. Equations (51) and (54) thus reduce the problem of evaluating the doubly-periodic 3D hydrodynamic Green’s functions to a much simpler scalar problem (56). Explicit expressions for the Wigner function and its multipolar projections are given in Appendix C. We also derive there Ewald sums for the hydrodynamic Green’s functions (55).

B. Average flow produced by a point force

The asymptotic periodic pressure Green’s function (55b) is proportional to the gradient of the periodic Wigner function w . Thus $\mathbf{Q}_{\text{HS}}^{\text{per}}$ is normalized to yield

zero average value over a unit cell (but any constant can be added without changing the system dynamics).

In contrast, the velocity Green’s function \mathbf{T}^{per} is fully determined by Eqs. (51a) and (55), with no gauge constants involved. Adding a constant would violate the boundary conditions on the channel walls—thus, the average flow field in a wall-bounded periodic system cannot be set independently. Instead, the average flow is a function of the applied pressure drop and the induced-force distribution (unlike the corresponding behavior in the infinite space).

As a key step in our analysis of suspension flow in a channel, we derive an expression for the average flow $\bar{\mathbf{u}}_0$ produced by a lateral point force \mathbf{F}_{\parallel} applied at a point $\mathbf{r}' = (\boldsymbol{\rho}', \mathbf{z}')$. (Only a lateral force needs to be considered, because a transverse force $\mathbf{F}_{\perp} = F_{\perp}\hat{\mathbf{e}}_z$ does not produce an average flow, by symmetry). The overall pressure drop in the system is assumed to vanish.

The average flow is given by the integral over a unit cell

$$\bar{\mathbf{u}}_0 = \Omega_{\text{p}}^{-1} \int_{\Omega_{\text{p}}} \mathbf{v}_0(\mathbf{r}) \, d\mathbf{r} \quad (57)$$

of the flow field

$$\mathbf{v}_0(\mathbf{r}) = \mathbf{T}^{\text{per}}(\mathbf{r}, \mathbf{r}') \cdot \mathbf{F}_{\parallel} \quad (58)$$

produced by the applied force. To determine the volume integral in Eq. (57) we use the decomposition (51a) of the Green’s function \mathbf{T}^{per} into the near-field and far-field components. The far-field contribution vanishes because

$$\int_{\Omega_{\text{p}}} \mathbf{T}_{\text{HS}}^{\text{per}}(\mathbf{r}, \mathbf{r}') = 0, \quad (59)$$

owing to Eq. (55a) and the periodicity of the pressure Green’s function $\mathbf{Q}_{\text{HS}}^{\text{per}}$. Therefore, the average flow $\bar{\mathbf{u}}_0$ is associated with the integral of the near-field contribution

$$\delta\mathbf{v}_0(\mathbf{r}) = \sum_{\mathbf{n}} \delta\mathbf{T}(\mathbf{r}, \mathbf{r}'_{\mathbf{n}}) \cdot \mathbf{F}_{\parallel} \quad (60)$$

over the unit cell Ω_{p} . Using the invariance of $\delta\mathbf{T}(\mathbf{r}, \mathbf{r}')$ with respect to lateral translations, this integral can be represented as

$$\bar{\mathbf{u}}_0 = \Omega_{\text{p}}^{-1} \int_{\Omega_{\text{p}}} \delta\mathbf{v}_0(\mathbf{r}) \, d\mathbf{r} = \Omega_{\text{p}}^{-1} \int_{\Omega_{\infty}} \delta\mathbf{T}(\mathbf{r}, \mathbf{r}') \cdot \mathbf{F}_{\parallel}, \quad (61)$$

where $\Omega_{\infty} = \sum_{\mathbf{n}} \Omega_{\text{p}}(\mathbf{n})$ is the whole infinite volume of the channel.

The integral (61) can be related to the dipolar strength (18) of the asymptotic pressure distribution (16) by inserting under the integration sign the identity tensor $\mathbf{I} = \nabla\mathbf{r}$ and integrating by parts. Since the boundary term vanishes, owing to the boundary conditions on the walls and the rapid decay of $\delta\mathbf{T}(\mathbf{r}, \mathbf{r}')$ for $\rho \rightarrow \infty$, we find that

$$\bar{\mathbf{u}}_0 = -\Omega_{\text{p}}^{-1} \int_{\Omega_{\infty}} \mathbf{r} \nabla \cdot \delta\mathbf{T}(\mathbf{r}, \mathbf{r}') \cdot \mathbf{F}_{\parallel} \, d\mathbf{r}. \quad (62)$$

Noting that the exact Green's function in Eq. (53a) is divergence-free and using relations (15), (16), and (20) for the asymptotic contribution we obtain the following fundamental result

$$\bar{\mathbf{u}}_0 = \kappa_0 \Omega_p^{-1} H \mathbf{D}_0, \quad (63)$$

where \mathbf{D}_0 is the dipole moment (18), and κ_0 is the permeability coefficient for the particle-free channel (10). In an explicit form we have

$$\bar{\mathbf{u}}_0 = \frac{1}{2} \eta^{-1} z' (H - z') \Omega_p^{-1} \mathbf{F}_\parallel. \quad (64)$$

Relation (64) is consistent with the average fluid velocity produced by a planar force distribution

$$f_s(\mathbf{r}) = \Omega_p^{-1} H \delta(z - z') \mathbf{F}_\parallel. \quad (65)$$

C. Average flow in the particle presence

The macroscopic fields $\nabla_\parallel \bar{p}$ and $\bar{\mathbf{u}}$ that appear in the effective-medium equations (49) and (50) can be identified with the volume averages of the microscopic pressure gradient $\nabla_\parallel p$ and velocity \mathbf{v} over a unit cell Ω_p ,

$$\nabla_\parallel \bar{p} = \Omega_p^{-1} \int_{\Omega_p} \nabla_\parallel p \, d\mathbf{r}, \quad (66a)$$

$$\bar{\mathbf{u}} = \Omega_p^{-1} \int_{\Omega_p} \mathbf{v} \, d\mathbf{r}. \quad (66b)$$

To determine the macroscopic transport coefficients in equations (49) and (50), we thus need to derive appropriate expressions for these averages.

In this section we consider a system of N particles at positions \mathbf{R}_i ($i = 1, \dots, N$) in the unit cell. The particles are represented by the corresponding induced-force distributions $\mathbf{F}_i(\mathbf{r})$.

It is convenient to represent the pressure and flow fields (12) (generalized to a multiparticle system) as the superpositions of the external and scattered contributions

$$p = p^{\text{ext}} + \sum_{i=1}^N p'_i, \quad (67a)$$

$$\mathbf{v} = \mathbf{v}^{\text{ext}} + \sum_{i=1}^N \mathbf{v}'_i. \quad (67b)$$

We assume that the applied pressure gradient ∇p^{ext} is constant in space and has only lateral components x and y . The corresponding external velocity field (27) depends only on the transverse coordinate z . The scattered flow and pressure fields \mathbf{v}' and p' are periodic, and they are given by the expressions

$$p'_i = \int_{\Omega_p} \mathbf{Q}^{\text{per}}(\mathbf{r}, \mathbf{r}') \cdot \mathbf{F}_i(\mathbf{r}') \, d\mathbf{r}', \quad (68a)$$

$$\mathbf{v}'_i = \int_{\Omega_p} \mathbf{T}^{\text{per}}(\mathbf{r}, \mathbf{r}') \cdot \mathbf{F}_i(\mathbf{r}') \, d\mathbf{r}'. \quad (68b)$$

By integrating the lateral gradient of the pressure (67a) over the unit cell Ω_p we find

$$\nabla_\parallel \bar{p} = \nabla p^{\text{ext}}, \quad (69)$$

where the integrals of the perturbation-pressure terms $\nabla_\parallel p'_i$ vanish by periodicity of p' . Equation (69) is important, because it allows us to express the macroscopic flow and particle motion in a channel in terms of the macroscopic pressure (rather than the external pressure) in the constitutive relations derived in Sec. VI.

Integrating relation (67b) with the external flow given by Eq. (27) yields

$$\bar{\mathbf{u}} = -\kappa_0 \nabla p^{\text{ext}} + \Omega_p^{-1} \sum_{i=1}^N \int_{\Omega_p} \mathbf{v}'_i(\mathbf{r}) \, d\mathbf{r}. \quad (70)$$

The integral on the right-hand-side of the above equation can be evaluated using the result (63) for the average velocity produced by a point force. Combining point-force results (57) and (58) with (68b), and taking into account that the transverse force components do not contribute to the average flow, we find

$$\bar{\mathbf{u}} = \kappa_0 (-\nabla p^{\text{ext}} + \Omega_p^{-1} H \sum_{i=1}^N \mathbf{D}_i), \quad (71)$$

where \mathbf{D}_i is the dipole moment (22) of particle i . Defining the average dipole moment

$$\bar{\mathbf{D}} = N^{-1} \sum_{i=1}^N \mathbf{D}_i, \quad (72)$$

relation (9) for the average flow is thus obtained.

According to the above derivation, equation (9) is valid for arbitrary particle densities, provided that the induced forces \mathbf{F}_i are evaluated with the multiparticle hydrodynamic interactions properly taken into account. In the low-density limit, the average dipole moment (72) can be expressed in terms of the dipole moment of an isolated particle $\mathbf{D}(Z)$,

$$\bar{n}_s \bar{\mathbf{D}} = \int_a^{H-a} n(Z) \mathbf{D}(Z) \, dZ, \quad (73)$$

where $n(Z)$ is the local particle number density per unit volume, averaged over the lateral position within a unit cell.

VI. TRANSPORT COEFFICIENTS

In this section we use the relation for the average velocity (9) to obtain the effective macroscopic equations for fluid and particle transport in a parallel-wall channel.

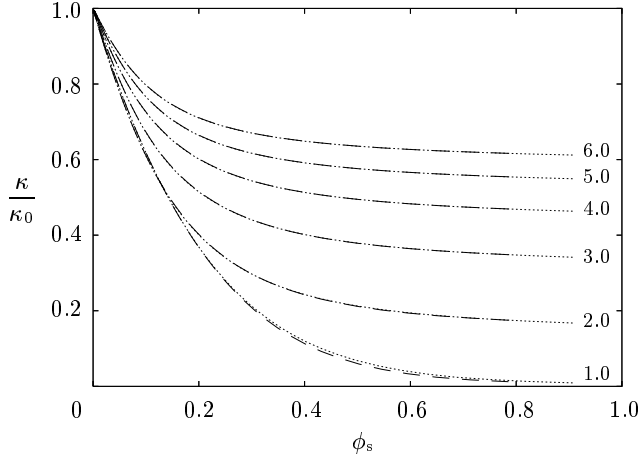


FIG. 5: Effective permeability (76) of a channel with a regular particle array adsorbed on the lower wall, versus area fraction ϕ_s , for several values of normalized channel width $H/(2a)$ (as labeled). Hexagonal particle arrangement (dotted lines); square arrangement (dashed lines).

In a dilute-suspension regime, the macroscopic transport equations are obtained by combining (9) with the friction relation (28) or mobility relation (36). At higher particle concentrations, we use (9) in combination with linear constitutive relations between the dipole moment and the macroscopic forcing for a system of interacting particles.

We consider here two important cases. In Sec. VI A we discuss fluid transport through a fixed bed of particles, and in Sec. VI B we examine transport of a suspension of freely moving particles.

A. Fixed bed of particles

1. Permeability coefficient

We begin our analysis of fluid transport through a fixed particle array by considering a low-density system. In the low-density domain, the dipole moment $\bar{\mathbf{D}}$ contribution to the average flow (9) can be obtained by averaging the polarizability component of the generalized resistance relation (28) over the particle distribution. Taking into account that $\mathbf{U} = \mathbf{\Omega} = 0$ we find that

$$\frac{1}{12}H^3\bar{\mathbf{D}} = \bar{\zeta}^{\text{PP}} \cdot \eta^{-1}\nabla_{\parallel}\bar{p}, \quad (74)$$

where

$$\bar{\zeta}^{\text{PP}} = \bar{n}_s^{-1} \int_a^{H-a} n(Z)\zeta^{\text{PP}}(Z) dZ \quad (75)$$

is the mean value of the ζ^{PP} component of the generalized resistance matrix in Eq. (28). The driving force in the polarizability relation (74) is the gradient of the macroscopic pressure $\nabla_{\parallel}\bar{p}$, which at low densities is identical to $\nabla_{\parallel}p^{\text{ext}}$. By inserting (74) into (9) we obtain

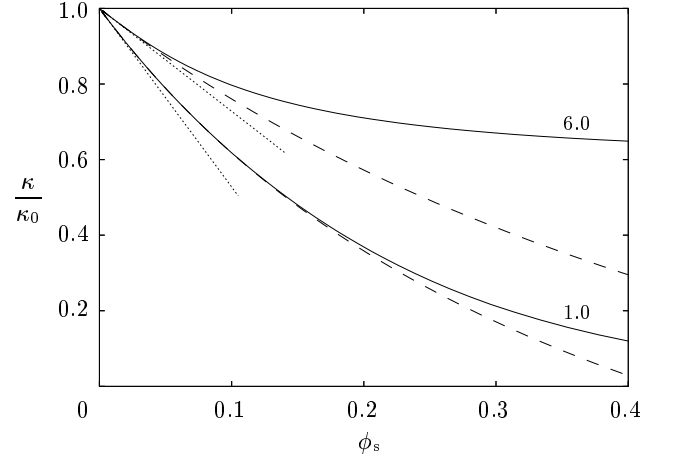


FIG. 6: Effective permeability (76) of a channel with a hexagonal particle array adsorbed on the lower wall, versus area fraction ϕ_s , for two values of normalized channel width $H/(2a)$ (as labeled). Exact result (solid lines); low-density limit (78) (dotted); Clausius-Mossotti approximation (79) (dashed).

Darcy's equation (49) with the permeability coefficient of the form

$$\kappa = \kappa_0(1 - 12\bar{n}_s H^{-3} \eta^{-1} \bar{\zeta}^{\text{PP}}), \quad (76)$$

where definition (10) was used to factor out the permeability of particle-free channel κ_0 .

The polarizability relation (74) and expression (76) for the channel permeability are valid not only for dilute-suspensions, but also for arbitrary particle concentrations, provided that the average (75) is replaced by the corresponding relation applicable in the high-concentration regime. As in other problems of field propagation through random media, the polarizability coefficient $\bar{\zeta}^{\text{PP}}$ can be expressed in terms of cluster integrals that involve pair, triplet, and higher-order resistance functions. Derivation of such a relation requires applying an appropriate renormalization procedure in which the external pressure is replaced by the macroscopic pressure in order to obtain absolutely convergent results for $\bar{\zeta}^{\text{PP}}$. Alternatively, we can get the polarizability from the dipole moment of particles in a channel with periodic boundary conditions in the lateral directions. Numerical results described in the following section have been obtained using the latter technique.

2. Numerical results

To illustrate the effect of immobile particles on the permeability of a parallel-wall channel we present results for a particle monolayer adsorbed on one of the walls. Figures 5–8 show the permeability coefficient (normalized by the permeability of a particle-free channel) for hexagonal and square particle arrays. For the square and hexagonal symmetry, the tensorial permeability coefficient is

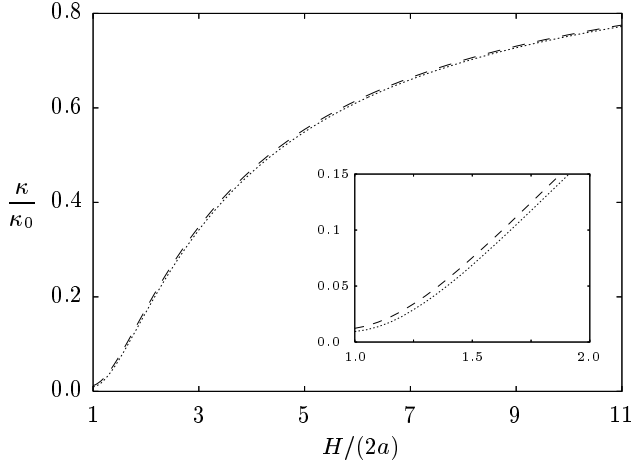


FIG. 7: Effective permeability (76) of a channel with a closed-packed regular particle array adsorbed on the lower wall, versus normalized channel width $H/(2a)$. Hexagonal particle arrangement (dotted lines); square arrangement (dashed lines). Inset shows a blowup of the plot for small values of $H/(2a)$.

isotropic

$$\kappa = \kappa \mathbf{l}_{\parallel}, \quad (77)$$

where \mathbf{l}_{\parallel} is the lateral unit tensor (21).

Figure 5 illustrates the dependence of the permeability coefficient κ on the particle area fraction $\phi_s = \bar{n}_s \pi a^2$ for several values of channel width. The results indicate that the permeabilities of the hexagonal and square arrays are nearly identical functions of ϕ_s —only for a channel with $H/(2a) \approx 1$ there is a noticeable difference, especially at high surface coverage ϕ_s .

In Fig. 6 our numerical results for hexagonal arrays are compared to the low-density limiting behavior

$$\frac{\kappa}{\kappa_0} = 1 - \tilde{\zeta}_1^{\text{pp}} \phi_s, \quad (78)$$

where the normalized one-particle polarizability coefficient $\tilde{\zeta}_1^{\text{pp}}$ is given by Eq. (43). Relation (78) follows from Eqs. (75) and (76) applied to a particle monolayer. For particles positioned in the midplane of the channel the particle density, averaged over the lateral directions, is $n(Z) = \bar{n}_s \delta(Z - \frac{1}{2}H)$, where $\bar{n}_s = N/(L_x L_y)$, and N denotes the number of particles in a unit cell. For more general particle distributions, the average value of $\tilde{\zeta}_1^{\text{pp}}$ would appear in (78).

In Fig. 6 we also plot the Clausius–Mossotti approximation

$$\frac{\kappa}{\kappa_0} = \frac{1 - \frac{1}{2} \tilde{\zeta}_1^{\text{pp}} \phi_s}{1 + \frac{1}{2} \tilde{\zeta}_1^{\text{pp}} \phi_s}, \quad (79)$$

which is a generalization of the classical electrostatic Clausius–Mossotti formula [28] to our present problem. The results indicate that for tightly confined systems

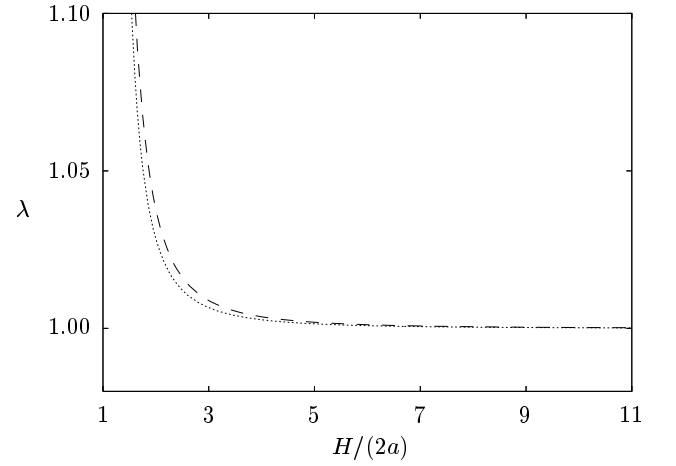


FIG. 8: Fluid-flux ratio (82) for the same two systems as those represented in Fig. 7.

with $H/(2a) \approx 1$, the approximation (79) is quite accurate in the area-fraction range $\phi_s \lesssim 0.2$. For weaker confinements, the range of validity of the Clausius–Mossotti formula is smaller.

The permeability of close-packed arrays (with the close-packing area fraction $\phi_s = \sqrt{3}\pi/6$ for hexagonal and $\phi_s = \pi/4$ for square ordering) is plotted in Fig. 7 versus the dimensionless wall separation $H/(2a)$. The results indicate that for $H/(2a) \approx 1$, the permeability coefficient is reduced to about 1% of the permeability κ_0 of a particle-free channel with the same width. Such a significant reduction of the channel permeability was observed in recent experiments [42].

At weaker confinements, the reduction of the permeability is much smaller, but it is still quite significant for $H/(2a) \lesssim 10$. For moderate and large channel widths the hindrance of fluid flow can be accurately accounted for in terms of the reduced effective channel width. In this approximation, the particle array is replaced by an equivalent solid slab of width Z_{NS} , occupying the region $0 \leq z \leq Z_{\text{NS}}$. The permeability of the narrowed channel is

$$\kappa_{\text{eff}} = \frac{1}{12} \eta^{-1} H_{\text{eff}}^2, \quad (80)$$

where

$$H_{\text{eff}} = H - Z_{\text{NS}} \quad (81)$$

is the effective channel width.

The accuracy of the effective-width approximation (80) can be estimated from a plot of the ratio

$$\lambda = \frac{H \kappa}{H_{\text{eff}} \kappa_{\text{eff}}} \quad (82)$$

of the fluid flux through the channel with adsorbed particles to the fluid flux through a particle-free channel of the reduced width. Such a plot is shown in Fig. 8 for closely packed hexagonal and square arrays. From our data we

find $Z_{\text{NS}} = 0.907$ for the hexagonal particle array and $Z_{\text{NS}} = 0.895$ for the square array. With the above values we get $\lambda \approx 1$ for $H/(2a) \gtrsim 2$. In this range of channel widths, the approximation that neglects the roughness of a densely packed particle layer adsorbed on the wall is thus accurate. We note that our findings are consistent with earlier investigations of fluid flow near rough surfaces [43, 44].

B. Suspension of freely moving particles

1. Macroscopic constitutive equation

The linear constitutive equation relating the macroscopic fluxes to macroscopic forces in the dilute-suspension regime is obtained by combining the dipolar expression for the average suspension velocity (9) with the generalized mobility relation (36). Relation (36) is first averaged over the particle distribution, which yields

$$\begin{bmatrix} \bar{\mathbf{U}} \\ \bar{\mathbf{\Omega}} \\ \frac{1}{12}\eta^{-1}H^3\bar{\mathbf{D}} \end{bmatrix} = \begin{bmatrix} \bar{\boldsymbol{\mu}}^{\text{tt}} & \bar{\boldsymbol{\mu}}^{\text{tr}} & \bar{\boldsymbol{\mu}}^{\text{tp}} \\ \bar{\boldsymbol{\mu}}^{\text{rt}} & \bar{\boldsymbol{\mu}}^{\text{rr}} & \bar{\boldsymbol{\mu}}^{\text{rp}} \\ \bar{\boldsymbol{\mu}}^{\text{pt}} & \bar{\boldsymbol{\mu}}^{\text{pr}} & -\bar{\boldsymbol{\mu}}^{\text{pp}} \end{bmatrix} \cdot \begin{bmatrix} \mathcal{F} \\ \mathcal{T} \\ -\nabla_{\parallel}\bar{p} \end{bmatrix}, \quad (83)$$

where

$$\bar{n}_s \bar{\boldsymbol{\mu}}_0^{AB} = \int_a^{H-a} n(Z) \boldsymbol{\mu}^{AB}(Z) dZ, \quad (84)$$

similar to Eq. (75) in the friction-representation case. In Eq. (83) it is assumed that the same force \mathcal{F} and torque \mathcal{T} act on all the particles in the system. We also assume that both \mathcal{F} and \mathcal{T} have only the lateral components. As it has been done for immobile particles, in Eq. (83) the external-pressure gradient is replaced with the gradient of the macroscopic pressure $\nabla_{\parallel}\bar{p}$ to obtain a local constitutive relation that can be generalized to dense systems.

By combining (9) and (83) we find

$$\begin{bmatrix} \bar{n}_s \bar{\mathbf{U}} \\ \bar{n}_s \bar{\mathbf{\Omega}} \\ H \bar{\mathbf{u}} \end{bmatrix} = \begin{bmatrix} \boldsymbol{\nu}^{\text{tt}} & \boldsymbol{\nu}^{\text{tr}} & \boldsymbol{\nu}^{\text{tp}} \\ \boldsymbol{\nu}^{\text{rt}} & \boldsymbol{\nu}^{\text{rr}} & \boldsymbol{\nu}^{\text{rp}} \\ \boldsymbol{\nu}^{\text{pt}} & \boldsymbol{\nu}^{\text{pr}} & \boldsymbol{\nu}^{\text{pp}} \end{bmatrix} \cdot \begin{bmatrix} \mathcal{F} \\ \mathcal{T} \\ -\nabla_{\parallel}\bar{p} \end{bmatrix}, \quad (85)$$

where

$$\boldsymbol{\nu}^{AB} = \bar{n}_s \bar{\boldsymbol{\mu}}^{AB}, \quad AB \neq \text{pp}, \quad (86a)$$

and

$$\boldsymbol{\nu}^{\text{pp}} = H\kappa_0(1 - 12\bar{n}_s H^{-3}\eta\bar{\boldsymbol{\mu}}^{\text{pp}}). \quad (86b)$$

In the constitutive relation (85), the macroscopic fluxes are: the particle flux $\bar{n}_s \bar{\mathbf{U}}$, particle angular flux $\bar{n}_s \bar{\mathbf{\Omega}}$, and the suspension volume flux $H \bar{\mathbf{u}}$.

Similar to the immobile-particle case, relations (83), (85), and (86) are valid at arbitrary densities, provided that the low-density formula (84) for the generalized mobility coefficients $\bar{\boldsymbol{\mu}}^{AB}$ is replaced with the corresponding expression that is appropriate at high densities.

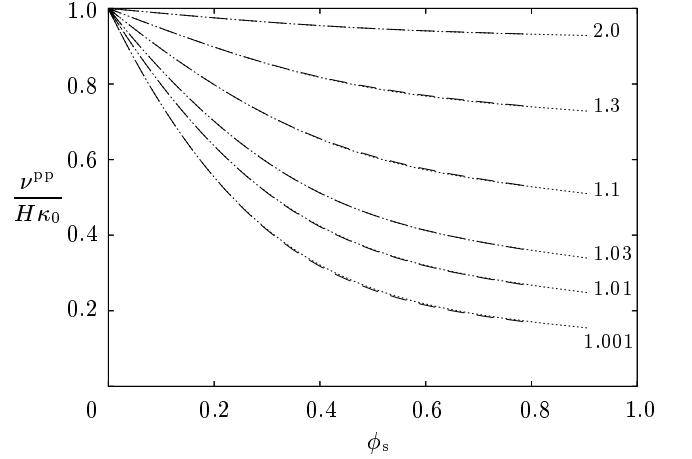


FIG. 9: Effective permeability (86b) of a channel with a regular particle array suspended in the midplane $Z = H/2$, versus area fraction ϕ_s , for several values of normalized channel width $H/(2a)$ (as labeled). Hexagonal particle arrangement (dotted lines); square arrangement (dashed lines).

2. Onsager reciprocal relations for the generalized mobility matrix $\boldsymbol{\nu}$

In Sec. IV we have shown that at low particle concentrations the generalized mobility/polarizability matrix $\boldsymbol{\mu}$ in Eq. (36) satisfies the Lorentz symmetry (8). The same symmetry also applies to the average defined by Eq. (84). It follows that the matrix of the kinetic coefficients (86) in the constitutive relation (85) satisfies the Onsager reciprocal relation

$$\boldsymbol{\nu}^{AB} = \boldsymbol{\nu}^{BA\dagger}. \quad (87)$$

While our derivation is given here only for dilute suspensions, one can show that the symmetry relation (87) is valid at arbitrary concentrations. The symmetry of the matrix $\boldsymbol{\nu}$ can be demonstrated using arguments similar to the ones given in Sec. IV, but applied to a periodic multiparticle system.

3. Numerical results

At low suspension concentrations and, more generally, for suspensions that are isotropic in the lateral directions, the transport coefficients $\boldsymbol{\nu}^{AB}$ are proportional to 2D isotropic tensors

$$\boldsymbol{\nu}^{\text{pt}} = \nu^{\text{pt}} \mathbf{I}_{\parallel}, \quad \boldsymbol{\nu}^{\text{pp}} = \nu^{\text{pp}} \mathbf{I}_{\parallel}, \quad (88a)$$

and

$$\boldsymbol{\nu}^{\text{pr}} = \nu^{\text{pr}} \boldsymbol{\epsilon}_{\parallel}, \quad (88b)$$

where $\boldsymbol{\epsilon}_{\parallel}$ is the lateral alternating tensor (42). Relations (88) are also satisfied for hexagonal and square particle lattices.

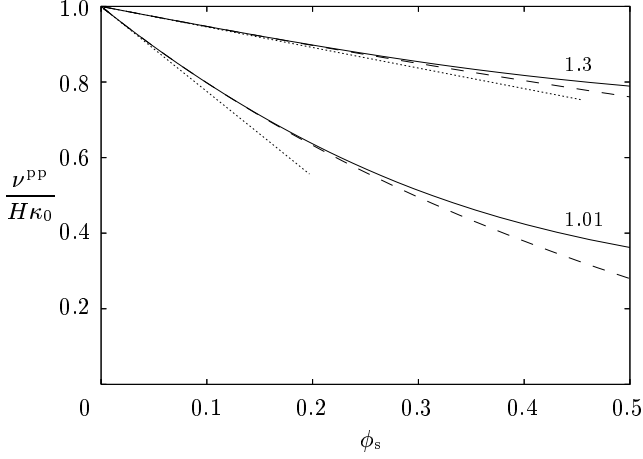


FIG. 10: Effective permeability (86b) of a channel with a hexagonal particle array freely suspended in the midplane $Z = H/2$, versus area fraction ϕ_s , for two values of normalized channel width $H/(2a)$ (as labeled). Exact result (solid lines); low-density limit (89) (dotted); Clausius-Mossotti approximation (90) (dashed).

The effective channel permeability coefficient ν^{PP} , normalized by the permeability of a particle-free channel, is plotted in Fig. 9 for infinite hexagonal and square particle arrays moving in the midplane of the channel. As for arrays of immobile particles, we find that the permeabilities of the square and hexagonal arrays with the same area fraction are nearly the same.

A comparison of the results depicted in Figs. 5 and 9 indicates that the permeability of a channel with particles freely suspended in the midplane $Z = H/2$ is much higher than the corresponding permeability of a channel where the particles are adsorbed at a wall. According to Fig. 9 the correction to the permeability due to the particle presence is below 10% in the regime $H/(2a) \gtrsim 2$, even for close-packed arrays. This result is consistent with the small value of the single-particle polarizability for a particle at the symmetry plane $Z = H/2$, as illustrated in Fig. 2. Both the small particle polarizability and the minor correction to the channel permeability stem from the small velocity gradient in the midplane of the channel, which implies that the suspended particles do not significantly perturb the fluid flow.

In Fig. 10 the results of the numerical calculations for periodic particle arrays are compared with the low-density expansion

$$\frac{\nu^{PP}}{H\kappa_0} = 1 - \tilde{\mu}_1^{PP} \phi_s, \quad (89)$$

where $\tilde{\mu}_1^{PP}$ is given by (45). We also plot the Clausius-Mossotti approximation

$$\frac{\nu^{PP}}{H\kappa_0} = \frac{1 - \frac{1}{2}\tilde{\mu}_1^{PP} \phi_s}{1 + \frac{1}{2}\tilde{\mu}_1^{PP} \phi_s}. \quad (90)$$

A comparison of the results shown in Figs. 6 and 10 in-

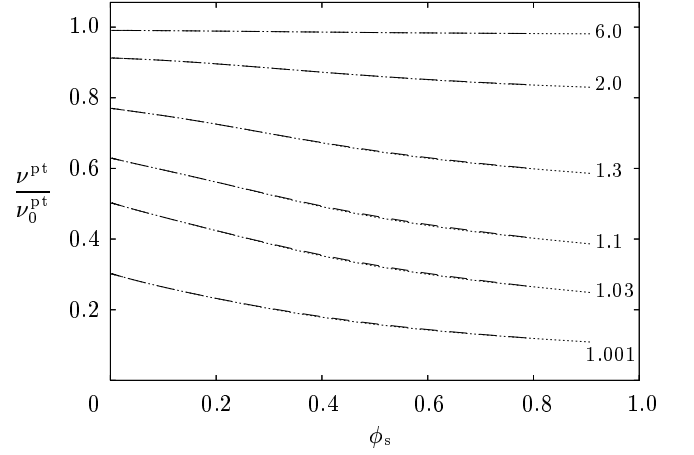


FIG. 11: Effective mobility coefficient ν^{Pt} for an infinite particle array in the midplane $Z = H/2$, normalized by the corresponding result for an array of point forces (91), versus area fraction ϕ_s , for several values of normalized channel width $H/(2a)$ (as labeled). Hexagonal particle arrangement (dotted lines); square arrangement (dashed lines). The coefficient ν^{Pt} describes the average suspension flow produced by a lateral force applied to the particle array.

indicate that the Clausius-Mossotti approximation has a broader range of validity for freely suspended particles than for the adsorbed ones.

The transport coefficients ν^{Pt} and ν^{Pr} , representing the average flow produced by a lateral force and torque acting on the particles, are plotted in Figs. 11 and 12. The transport coefficients are shown normalized by the respective results

$$\nu_0^{Pt} = \bar{n}_s \mu_0^{Pt}(Z), \quad (91)$$

$$\nu_0^{Pr} = \bar{n}_s \mu_0^{Pr}(Z) \quad (92)$$

for the average flow produced by arrays of point forces and torques applied to the suspending fluid at the particle positions Z , where μ_0^{Pt} and μ_0^{Pr} are given by relations (47) and (48). The results are presented for square and hexagonal particle arrays. For the system driven by the lateral force, the particles are in the midplane of the channel $Z = H/2$. For the lateral torque the rotational mobility coefficient ν^{Pr} is shown for $Z = a + \frac{1}{3}(H - 2a)$, because the torque applied to the particles produces average flow only for off-center positions.

The results in Fig. 11 indicate that for $H/(2a) \gtrsim 2$ the average flow produced in a channel by an external force applied to the particles is well represented by the point-force approximation (91), even for dense particle arrays. The normalized average flow in this regime is insensitive both to the dimensionless channel width $H/(2a)$ and to the area fraction ϕ_s . For smaller values of $H/(2a)$, the normalized average flow is smaller than the flow produced by point forces. However, a significant deviation of the

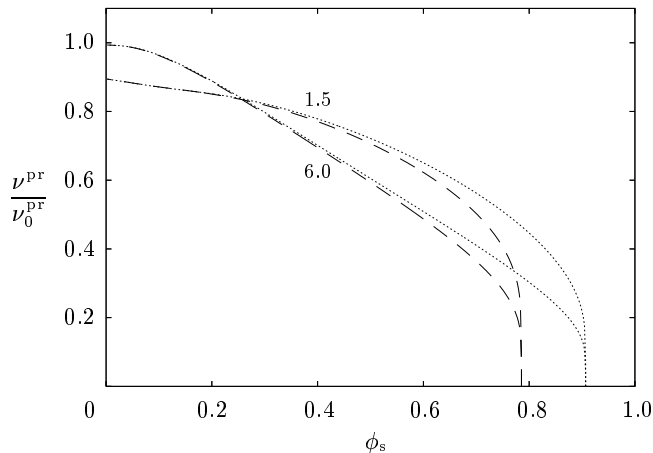


FIG. 12: Effective mobility coefficient ν^{Pr} for an infinite particle array in the plane $Z = a + \frac{1}{3}(H - 2a)$, normalized by the corresponding results for an array of point torques (92), versus area fraction ϕ_s , for several values of normalized channel width $H/(2a)$ (as labeled). Hexagonal particle arrangement (dotted lines); square arrangement (dashed lines). The coefficient ν^{Pr} describes the average suspension flow produced by a lateral torque applied to the particle array.

normalized transport coefficient $\nu^{\text{Pt}}/\nu_0^{\text{Pt}}$ from unity is observed only for particles with the diameter nearly equal to the channel width. This behavior is similar to the one seen in Fig. 9 for arrays driven by an external pressure gradient. The low-density values are consistent with the one-particle results represented in Fig. 3. The results for hexagonal and square lattices for a given area fraction are nearly indistinguishable.

As depicted in Fig. 12, the average flow produced by a torque \mathcal{T} applied to the particles strongly depends on the particle area fraction, even for large wall separations. This is because particle rotation involves relative motion of the surfaces of the spheres, whereas the motion of force-driven particle monolayers does not involve any relative particle displacements. Moreover, we find that the results for the square and hexagonal particle arrays are significantly different for $\phi_s \gtrsim 0.5$. The transport coefficient ν^{Pr} vanishes at the close-packing area fraction for a given system geometry, because the particle rotation is arrested by the lubrication forces between the touching particles. In the low-density regime the results are independent of the particle lattice. The low-density values of the transport coefficients are equivalent to the one-particle results represented in Fig. 4.

VII. CONCLUSIONS

We have presented a detailed analysis of the far-field scattered flow produced by spherical particles in Stokes flow bounded by two parallel planar walls. Furthermore, we have examined the effect of the far-field particle re-

sponse to external forcing on the macroscopic suspension flow. Both the permeability of a system of fixed particles in a channel and the macroscopic dynamics of a suspension of freely moving particles were analyzed. (We note that related ideas were also explored in [45], in the context of molecular-dynamics simulations of the motion of nano-particles in a confined fluid.)

For a system of fixed particles, the macroscopic fluid flux is related to the macroscopic pressure via linear Darcy's law. We have shown that for a given macroscopic pressure gradient, the difference between the fluid flux in the particle presence and in a particle-free channel can be expressed in terms of the effective 2D dipole moment characterizing the amplitude of the far-field Hele-Shaw dipolar scattered flow produced by the particles. From this amplitude we have evaluated the particle contribution to the effective permeability coefficient.

A similar physical picture also applies to the flow of a suspension in a channel. However, in this case the macroscopic volume flux can be produced not only by the macroscopic pressure gradient but also by the external force or torque applied to the particles. There are also particle fluxes corresponding to the linear and angular particle velocities. Therefore, the constitutive relation for suspension flow through a channel involves three forcing and three flux components. The macroscopic fluxes and driving force are related through a 3×3 matrix of (generally tensorial) transport coefficients. We have demonstrated that, with a proper normalization, this matrix is symmetric, i.e., the transport coefficients satisfy the Onsager reciprocal relations.

Our theoretical analysis has been supplemented by numerical results for transport coefficients describing dynamics of square and hexagonal particle arrays (for particle monolayers adsorbed on a wall and monolayers of freely suspended particles). We have shown that dense arrays of tightly confined particles can reduce fluid flow through a channel by as much as 99%.

We have also proposed generalized Clausius-Mossotti formulas for the channel permeability, both for fixed and freely suspended particles. These formulas are analogous to the well-known electrostatic Clausius-Mossotti approximation. At moderate particle concentrations, our expressions agree well with the numerical calculations, especially for tightly confined particle arrays.

Our numerical results for the transport coefficients characterizing macroscopic motion of regular particle arrays can be used to describe the macroscopic deformation of finite-size regular 2D particle clusters. As we have shown in our recent paper [20], such arrays exhibit a complex nonlinear dynamics that involves rearrangements of a deformed particle lattice. There are also order-disorder transitions resulting from lattice instabilities. In future publications we will analyze these problems using the macroscopic theory developed in this paper. We will also determine particle and fluid transport in suspensions of randomly distributed particles.

Our analysis of suspension flow in parallel-wall chan-

nels with periodic boundary conditions has also provided another important result: we have derived explicit Ewald-summation formulas for the flow and pressure periodic Green's functions in the parallel-wall geometry. These formulas can be applied in Stokesian-dynamics and boundary-integral simulations of suspension and emulsion flows in narrow channels and slit pores, and in studies of the dynamics of confined macromolecules.

In future publications we will discuss the effect of the far-field flow on the dynamics of macromolecules (e.g., polymer chains). Earlier studies have suggested that in a confined system the far-field contribution to the hydrodynamic interactions between the chain segments can be neglected, because, on average, this contribution vanishes by symmetry [46, 47]. Our preliminary investigation based on the present results indicates that the role of the far-field flow is much more subtle, although the far-field hydrodynamic interactions do not change the Rouse scaling exponent for the longest relaxation time (only the prefactor is affected).

Acknowledgments

We would like to acknowledge numerous useful discussions with S. Bhattacharya at the early stages of this project. We also acknowledge his contribution to the derivation of the expressions for periodic Green's functions, presented in Appendix C. This work was supported by NSF CAREER grant CTS-0348175; EW was also supported by Polish Ministry of Science grant N501 020 32/1994.

APPENDIX A: VELOCITY AND PRESSURE GREEN'S FUNCTIONS \mathbf{T} AND \mathbf{Q}

In this Appendix we present our explicit expressions for the velocity and pressure Green's functions \mathbf{T} and \mathbf{Q} for Stokes flow between two parallel planar walls. The ex-

pressions are obtained using our Cartesian-representation approach introduced in [3, 4]. In our previous papers explicit results were given only for multipolar projections of the Green's tensor \mathbf{T} .

The Green's functions for Stokes flow between two parallel walls can be expressed as a sum of the free-space part and the wall contribution,

$$\mathbf{T}(\mathbf{r}, \mathbf{r}') = \mathbf{T}_0(\mathbf{r} - \mathbf{r}') + \mathbf{T}'(\mathbf{r}, \mathbf{r}') \quad (\text{A1a})$$

$$\mathbf{Q}(\mathbf{r}, \mathbf{r}') = \mathbf{Q}_0(\mathbf{r} - \mathbf{r}') + \mathbf{Q}'(\mathbf{r}, \mathbf{r}') \quad (\text{A1b})$$

where

$$\mathbf{T}_0(\mathbf{r}) = \frac{1}{8\pi\eta r}(\hat{\mathbf{I}} + \mathbf{r}\mathbf{r}), \quad \mathbf{Q}_0(\mathbf{r}) = \frac{1}{8\pi\eta r} \quad (\text{A2})$$

are the Oseen tensor and the corresponding pressure Green's function. As in [3, 4] the wall contributions to the Green's functions, \mathbf{T}' and \mathbf{Q}' , are represented in terms of lateral Fourier integrals of simple matrix products.

It is convenient to express components of the tensor \mathbf{T}' and vector \mathbf{Q}' in terms of the spherical basis of unit vectors [48]

$$\hat{\mathbf{e}}_{-1} = \frac{1}{\sqrt{2}}(\hat{\mathbf{e}}_x - i\hat{\mathbf{e}}_y), \quad \hat{\mathbf{e}}_0 = \hat{\mathbf{e}}_z, \quad \hat{\mathbf{e}}_1 = -\frac{1}{\sqrt{2}}(\hat{\mathbf{e}}_x + i\hat{\mathbf{e}}_y). \quad (\text{A3})$$

Accordingly, we have

$$\mathbf{T}'(\mathbf{r}_1, \mathbf{r}_2) = \sum_{m=-1}^1 \sum_{m'=-1}^1 T'_{mm'}(\mathbf{r}_1, \mathbf{r}_2) \hat{\mathbf{e}}_m \hat{\mathbf{e}}_{m'}^*, \quad (\text{A4a})$$

$$\mathbf{Q}'(\mathbf{r}_1, \mathbf{r}_2) = \sum_{m'=-1}^1 Q'_{m'}(\mathbf{r}_1, \mathbf{r}_2) \hat{\mathbf{e}}_{m'}^*. \quad (\text{A4b})$$

The components $T'_{mm'}$ and $Q'_{m'}$ can be evaluated from the following 2D Fourier integrals

$$T'_{mm'}(\mathbf{r}_1, \mathbf{r}_2) = -\frac{i^{m'-m}}{8\pi\eta} \int t_{mm'}(k; z_1, z_2) e^{i(m'-m)\psi} e^{i\mathbf{k} \cdot \boldsymbol{\rho}_{12}} \frac{d\mathbf{k}}{2\pi k}, \quad (\text{A5a})$$

$$Q'_{m'}(\mathbf{r}_1, \mathbf{r}_2) = -\frac{i^{m'}}{4\pi} \int q_{m'}(k; z_1, z_2) e^{im'\psi} e^{i\mathbf{k} \cdot \boldsymbol{\rho}_{12}} \frac{d\mathbf{k}}{2\pi k}, \quad (\text{A5b})$$

where $\boldsymbol{\rho}_{12} = \boldsymbol{\rho}_1 - \boldsymbol{\rho}_2$, and $\mathbf{k} = (k, \psi)$ represents the wave vector \mathbf{k} in polar coordinates. The integral kernels in Eqs. (A5) can be expressed as products of several simple

matrices,

$$t_{mm'}(k; z_1, z_2) = \mathbf{B}^\dagger(z_1, k, m) \cdot \tilde{\mathbf{Z}}_{\text{TW}}(\mathbf{k}) \cdot \mathbf{B}(z_2, k, m'), \quad (\text{A6a})$$

$$q_{m'}(k; z_1, z_2) = \mathbf{b}^\dagger(z_1, k) \cdot \tilde{\mathbf{Z}}_{\text{TW}}(\mathbf{k}) \cdot \mathbf{B}(z_2, k, m'), \quad (\text{A6b})$$

where the dagger denotes the transpose.

As explained in [3, 4], the matrix

$$\tilde{\mathbf{Z}}_{\text{TW}}(\mathbf{k}) = \begin{bmatrix} \mathbf{Z}_w^{-1} & \tilde{\mathbf{S}}_C^{++}(-kH) \\ \tilde{\mathbf{S}}_C^{--}(kH) & \mathbf{Z}_w^{-1} \end{bmatrix}^{-1} \quad (\text{A7})$$

describes the multiple reflections of Cartesian hydrodynamic basis fields from the parallel walls. The 3×3 component displacement matrices

$$\tilde{\mathbf{S}}_C^{++}(-kH) = [\tilde{\mathbf{S}}_C^{--}(kH)]^\dagger = \begin{bmatrix} 1 & 0 & -2kH \\ 0 & 1 & 0 \\ 0 & 0 & 1 \end{bmatrix} e^{-kH} \quad (\text{A8})$$

describe the propagation of the flow fields between the walls, and the matrices

$$\mathbf{Z}_w = \begin{bmatrix} 1 & 0 & 0 \\ 0 & 1 & 0 \\ 0 & 0 & 1 \end{bmatrix} \quad (\text{A9})$$

represent scattering of the flow field from the walls. The matrices

$$\mathbf{B}(k, z, m) = [2(1-m)!(1+m)!]^{-1/2} \begin{bmatrix} \mathbf{B}^L(k, z, m) \\ \mathbf{B}^U(k, z, m) \end{bmatrix} \quad (\text{A10})$$

where

$$\mathbf{B}^L(k, z, m) = (-1)^{m+1} e^{-kz} \begin{bmatrix} -2kz + 2m^2 - 1 \\ 2m \\ 1 \end{bmatrix}, \quad (\text{A11a})$$

$$\mathbf{B}^U(k, z, m) = e^{-k(H-z)} \begin{bmatrix} 1 \\ 2m \\ -2k(H-z) + 2m^2 - 1 \end{bmatrix}, \quad (\text{A11b})$$

describe the expansion of the Stokeslet into Cartesian basis fields centered at the positions of the lower and upper wall. Finally,

$$\mathbf{b}(k, z) = 2^{1/2} k \begin{bmatrix} \mathbf{b}^L(k, z) \\ \mathbf{b}^U(k, z) \end{bmatrix} \quad (\text{A12})$$

where

$$\mathbf{b}^L(k, z) = e^{-kz} \begin{bmatrix} 1 \\ 0 \\ 0 \end{bmatrix}, \quad (\text{A13a})$$

$$\mathbf{b}^U(k, z) = e^{-k(H-z)} \begin{bmatrix} 0 \\ 0 \\ 1 \end{bmatrix}, \quad (\text{A13b})$$

correspond to the pressure (at point z), associated with the Cartesian basis fields centered at the lower or upper wall. The three components in the matrices (A8), (A9),

(A11), and (A13) correspond to the pressure, vorticity, and potential basis solutions of Stokes equations.

The 2D Fourier integrals (A5) can be converted into the 1D Hankel transforms by performing the angular integration with the help of the relation

$$(2\pi)^{-1} \int_0^{2\pi} e^{im\psi} e^{i\mathbf{k} \cdot \boldsymbol{\rho}_{12}} d\psi = i^m e^{im\varphi_{12}} J_m(k\rho_{12}), \quad (\text{A14})$$

where φ_{12} is the polar angle of the vector $\boldsymbol{\rho}_{12}$, and $J_m(x)$ is the Bessel function of the order m . The resulting expressions are

$$\mathbf{T}'_{mm'}(\mathbf{r}_1, \mathbf{r}_2) = (-1)^{m'-m} e^{i(m'-m)\varphi_{12}} \tilde{t}_{mm'}(\mathbf{r}_1, \mathbf{r}_2), \quad (\text{A15a})$$

$$\mathbf{Q}'_{m'}(\mathbf{r}_1, \mathbf{r}_2) = (-1)^{m'} e^{im'\varphi_{12}} \tilde{q}_{m'}(\mathbf{r}_1, \mathbf{r}_2), \quad (\text{A15b})$$

where

$$\tilde{t}_{mm'}(\mathbf{r}_1, \mathbf{r}_2) = -\frac{1}{8\pi\eta} \int_0^\infty t_{mm'}(k; z_1, z_2) J_{m'-m}(k\rho_{12}) dk, \quad (\text{A16a})$$

$$\tilde{q}_{m'}(\mathbf{r}_1, \mathbf{r}_2) = -\frac{1}{4\pi} \int_0^\infty q_{m'}(k; z_1, z_2) J_{m'}(k\rho_{12}) dk. \quad (\text{A16b})$$

Substituting (A15) into (A4) and using definitions (A3) of the spherical basis vectors we get

$$\begin{aligned} \mathbf{T}'(\mathbf{r}_1, \mathbf{r}_2) &= \tilde{t}_{11}(\mathbf{r}_1, \mathbf{r}_2) \mathbf{l}_\parallel + \tilde{t}_{1-1}(\mathbf{r}_1, \mathbf{r}_2) (\mathbf{l}_\parallel - 2\hat{\boldsymbol{\rho}}_{12}\hat{\boldsymbol{\rho}}_{12}) \\ &\quad + \sqrt{2}[\tilde{t}_{01}(\mathbf{r}_1, \mathbf{r}_2)\hat{\mathbf{e}}_z\hat{\boldsymbol{\rho}}_{12} + \tilde{t}_{10}(\mathbf{r}_1, \mathbf{r}_2)\hat{\boldsymbol{\rho}}_{12}\hat{\mathbf{e}}_z] \\ &\quad + \tilde{t}_{00}(\mathbf{r}_1, \mathbf{r}_2)\hat{\mathbf{e}}_z\hat{\mathbf{e}}_z, \end{aligned} \quad (\text{A17a})$$

$$\mathbf{Q}'_{m'}(\mathbf{r}_1, \mathbf{r}_2) = \sqrt{2}\tilde{q}_1(\mathbf{r}_1, \mathbf{r}_2)\hat{\boldsymbol{\rho}}_{12} + \tilde{q}_0(\mathbf{r}_1, \mathbf{r}_2)\hat{\mathbf{e}}_z. \quad (\text{A17b})$$

We note that relations (A4)–(A17) for the Green's functions \mathbf{T} and \mathbf{Q} are equivalent to those derived by Jones [2], but our expressions are more transparent. In particular, the dependence of the integrands on the variables z_1 and z_2 is clearly factored out, because z appears only in the matrices (A10) and (A12). Moreover, our expressions can easily be adapted to other boundary conditions at the walls (e.g., a fluid–fluid interface) by simply replacing the reflection matrix \mathbf{Z}_w .

APPENDIX B: TRANSFORMATION VECTORS

$\mathbf{X}(A | lm\sigma)$ AND $\mathbf{X}(lm\sigma | A)$

In this Appendix we give explicit expressions for the transformational vectors $\mathbf{X}(A | lm\sigma)$ (where $A = \text{t}, \text{r}, \text{p}$), defined in Eqs. (30) and (31). Formulas for translational and rotational transformation vectors $\mathbf{X}(\text{t} | lm\sigma)$, $\mathbf{X}(lm\sigma | \text{t})$, $\mathbf{X}(\text{r} | lm\sigma)$, and $\mathbf{X}(lm\sigma | \text{r})$ were derived in [4]. The transformation vector $\mathbf{X}(lm\sigma | \text{p})$ (in a slightly different notation) is given in [5]. The remaining transformation vector $\mathbf{X}(\text{p} | lm\sigma)$ can be directly obtained from relations (50)–(52) in Ref. [23].

The transformation vectors \mathbf{X} in Eqs. (30) are given by the expressions

$$\mathbf{X}(t | l m \sigma) = (\frac{4}{3}\pi)^{1/2} \delta_{l1} \delta_{\sigma 0} \hat{\mathbf{e}}_m \quad (\text{B1a})$$

$$\mathbf{X}(r | l m \sigma) = -2i(\frac{4}{3}\pi)^{1/2} \delta_{l1} \delta_{\sigma 1} \hat{\mathbf{e}}_m \quad (\text{B1b})$$

$$\mathbf{X}(p | l m \sigma) = 2^{-1/2} m C(Z; l m \sigma) \hat{\mathbf{e}}_m, \quad (\text{B1c})$$

where $\hat{\mathbf{e}}_m$ denote the basis vectors (A3), and $m = -1, 0, 1$. For other values of m , the transformation vectors vanish. It can be verified that the reciprocal trans-

formation vectors $\mathbf{X}(l m \sigma | A)$ are related to (B1) via the symmetry (32).

The transformation vector $\mathbf{X}(p | l m \sigma)$ is nonzero only for $m = \pm 1$ and

$$l + \sigma \leq 3. \quad (\text{B2})$$

The coefficient C in relation (B1c) can be expressed in the form [23]

$$C(Z; l \pm 1 \sigma) = B_{l-1 \sigma}^{\pm}(1; Z), \quad (\text{B3})$$

where $B_{\lambda \sigma}^{\pm}(1; Z)$ denote the elements of the 3×3 matrix

$$\{B_{\lambda \sigma}^{\pm}(1; Z)\}_{\lambda, \sigma=0,1,2} = \mp \left(\frac{2\pi}{3}\right)^{1/2} \begin{bmatrix} -Z(H-Z) & \mp(H-2Z) & 2 \\ \frac{-(H-2Z)}{2\sqrt{5}} & \pm \frac{1}{\sqrt{5}} & 0 \\ \frac{2}{15\sqrt{3}} & 0 & 0 \end{bmatrix}. \quad (\text{B4})$$

The range $\lambda = 0, 1, 2$ of the index $\lambda = l - 1$ in equation (B4) results from the conditions $l \geq 1$ and (B2).

APPENDIX C: FAR-FIELD CONTRIBUTIONS TO PERIODIC GREEN'S FUNCTIONS

In this Appendix we list explicit formulas for the far-field contributions to periodic Green's functions for Stokes flow between two parallel walls. In Sec. C 1 we first consider the 2D scalar problem. We provide an Ewald-sum representation for the Wigner function w and list the corresponding expressions for the periodic multipolar solutions of Laplace equation in 2D. In Sec. C 2 we give explicit formulas for the periodic Green's function (55) and for their spherical matrix elements (25).

1. Multipolar periodic solutions of 2D Laplace equation

The relations presented in this sections are based on the results of Cichocki and Felderhof [41] who have derived Ewald-type expressions for the 2D periodic multipolar potentials.

a. Wigner function

As shown in [41], Wigner function can be represented by the following formula

$$w(\boldsymbol{\rho}) = \frac{1}{2} \sum_{\mathbf{n}} E_1 \left(\frac{\pi |\boldsymbol{\rho} - \boldsymbol{\rho}_{\mathbf{n}}|^2}{\sigma^2} \right) + \frac{1}{2\pi L_x L_y} \sum_{\mathbf{n} \neq 0} \frac{1}{k_{\mathbf{n}}^2} \exp(-\pi \sigma^2 k_{\mathbf{n}}^2 + 2\pi i \mathbf{r} \cdot \mathbf{k}_{\mathbf{n}}) - \frac{\sigma^2}{2L_x L_y} + C_w. \quad (\text{C1})$$

Here

$$\boldsymbol{\rho}_{\mathbf{n}} = n_x L_x \hat{\mathbf{e}}_x + n_y L_y \hat{\mathbf{e}}_y, \quad (\text{C2a})$$

$$\mathbf{k}_{\mathbf{n}} = \frac{n_x}{L_x} \hat{\mathbf{e}}_x + \frac{n_y}{L_y} \hat{\mathbf{e}}_y \quad (\text{C2b})$$

are the direct and reciprocal lattice vectors,

$$E_1(x) = \int_1^\infty \frac{e^{-xt}}{t} dt \quad (\text{C3})$$

is the exponential function, and σ is the splitting parameter that controls the convergence of the direct and

reciprocal sums. The gauge constant $C_w = 1.3105329259$ [41] is used to set the limit

$$\lim_{\boldsymbol{\rho} \rightarrow \boldsymbol{\rho}_n} [w(\boldsymbol{\rho}) - \Phi_0^-(\boldsymbol{\rho} - \boldsymbol{\rho}_n)] = 0. \quad (\text{C4})$$

b. Multipolar solutions

The periodic multipolar solutions $\tilde{\Phi}_m^-$ of the 2D Laplace equation are defined in terms of the non-periodic multipolar basis fields

$$\Phi_0^-(\boldsymbol{\rho}) = -\ln \rho, \quad \Phi_m^-(\boldsymbol{\rho}) = \frac{1}{2|m|} \rho^{-|m|} e^{im\phi}, \quad m \neq 0, \quad (\text{C5a})$$

$$\Phi_m^+(\boldsymbol{\rho}) = \rho^{|m|} e^{im\phi}. \quad (\text{C5b})$$

By definition, for $m = 0$ we simply have

$$\tilde{\Phi}_0^-(\boldsymbol{\rho}) \equiv w(\boldsymbol{\rho}). \quad (\text{C6})$$

For nonzero values of m , the multipolar solutions are given by the expression

$$\tilde{\Phi}_m^-(\boldsymbol{\rho}) = \frac{1}{\Gamma(|m|)} \sum_{\mathbf{n}} \Gamma(|m|, \pi\sigma^{-2}|\boldsymbol{\rho} - \boldsymbol{\rho}_n|^2) \Phi_m^-(\boldsymbol{\rho} - \boldsymbol{\rho}_n) + \frac{\pi^{|m|-1} i^{|m|}}{2|m|! L_x L_y} \sum_{\mathbf{n} \neq 0} k_{\mathbf{n}}^{-2} \Phi_m^+(\mathbf{k}_{\mathbf{n}}) \exp(-\pi\sigma^2 k_{\mathbf{n}}^2 + 2\pi i \boldsymbol{\rho} \cdot \mathbf{k}_{\mathbf{n}}), \quad (\text{C7})$$

where $\Gamma(j, x)$ is the incomplete Gamma function.

Near the singularities at the lattice points $\boldsymbol{\rho} = \boldsymbol{\rho}_n$ the periodic functions (C7) behave as

$$\tilde{\Phi}_m^-(\boldsymbol{\rho}) \simeq \Phi_m^-(\boldsymbol{\rho} - \boldsymbol{\rho}_n). \quad (\text{C8})$$

For $|m| > 0$ the gauge constants are determined by the condition that the fields $\tilde{\Phi}_m^-(\boldsymbol{\rho})$ can be expressed as combinations of derivatives of the Wigner function $w(\boldsymbol{\rho})$.

where the first term on the right-hand side corresponds to the background term in the periodic Poisson equation (56). Setting $\bar{\boldsymbol{\rho}} = \boldsymbol{\rho}' - \boldsymbol{\rho}_{12}$ and using relations

c. Displacement theorems

The multipolar fields (C7) can be used to construct the displacement formula for the Wigner potential [41]

$$w(\boldsymbol{\rho} + \bar{\boldsymbol{\rho}}) = \frac{\pi}{2L_x L_y} \bar{\rho}^2 + \sum_{m_1=-\infty}^{\infty} \tilde{\Phi}_{m_1}^-(\boldsymbol{\rho}) \Phi_{m_1}^{+*}(\bar{\boldsymbol{\rho}}), \quad (\text{C9})$$

$$\Phi_{m_1}^{+*}(\boldsymbol{\rho} - \boldsymbol{\rho}') = \sum_{\substack{m, m' \\ m+m'=m_1}} (-1)^m \theta(mm') \frac{(|m| + |m'|)!}{|m|! |m'|!} \Phi_{-m}^+(\boldsymbol{\rho}) \Phi_{m'}^{+*}(\boldsymbol{\rho}'), \quad (\text{C10})$$

[where $\theta(x)$ is the Heaviside step function] and

$$2\boldsymbol{\rho} \cdot \boldsymbol{\rho}' = \Phi_1^+(\boldsymbol{\rho}) \Phi_1^{+*}(\boldsymbol{\rho}') + \Phi_{-1}^+(\boldsymbol{\rho}) \Phi_{-1}^{+*}(\boldsymbol{\rho}') \quad (\text{C11})$$

we find a symmetric displacement relation

$$w(\boldsymbol{\rho} + \boldsymbol{\rho}_{12} - \boldsymbol{\rho}') = \frac{\pi}{2L_x L_y}(\rho^2 + \rho'^2) + \sum_{m=-\infty}^{\infty} \sum_{m'=-\infty}^{\infty} \Phi_m^+(\boldsymbol{\rho}) \tilde{S}_{\text{cyl}}^{+-}(\boldsymbol{\rho}_{12}; m \mid m') \Phi_{m'}^{+*}(\boldsymbol{\rho}'), \quad (\text{C12})$$

where

$$\tilde{S}_{\text{cyl}}^{+-}(\boldsymbol{\rho}_{12}; m \mid m') = -\frac{\pi}{2L_x L_y}(\delta_{1m}\delta_{1m'} + \delta_{-1m}\delta_{-1m'}) + \theta(-mm')(-1)^{m'} \frac{(|m| + |m'|)!}{|m|!|m'|!} \tilde{\Phi}_{m'-m}^-(\boldsymbol{\rho}_{12}) \quad (\text{C13})$$

is the displacement matrix for periodic multipolar scalar fields. Integrating the above expressions with the multipolar source distribution of order m' , centered at $\boldsymbol{\rho}' = 0$ yields the displacement theorem for the multipolar periodic solutions (C7),

$$\tilde{\Phi}_{m'}^-(\boldsymbol{\rho} + \boldsymbol{\rho}_1) = \delta_{m0} \frac{\pi}{2L_x L_y} \rho_1^2 + \sum_{m=-\infty}^{\infty} \Phi_m^+(\boldsymbol{\rho}_1) \tilde{S}_{\text{cyl}}^{+-}(\boldsymbol{\rho}; m \mid m'), \quad (\text{C14})$$

where the convergence condition $\rho_1 < \rho$ is assumed.

2. Asymptotic Green's functions for Stokes flow

a. Green's functions $\mathbf{T}_{\text{HS}}^{\text{per}}$ and $\mathbf{Q}_{\text{HS}}^{\text{per}}$

The relations given in the previous section can be used to derive explicit expressions for the asymptotic Green's functions (55). Taking the gradients of relation (C12) with respect to variables $\boldsymbol{\rho}$ and $\boldsymbol{\rho}'$, and evaluating the results at $\boldsymbol{\rho} = \boldsymbol{\rho}' = 0$ we find

$$\mathbf{T}_{\text{HS}}^{\text{per}}(\mathbf{r}_1, \mathbf{r}_2) = -\frac{3}{\pi\eta H^3} z_1(H - z_1)z_2(H - z_2) \sum_{m=-1,1} \sum_{m'=-1,1} mm' \tilde{S}_{\text{cyl}}^{+-}(\boldsymbol{\rho}_{12}; m \mid m') \hat{\mathbf{e}}_m \hat{\mathbf{e}}_{m'}^*, \quad (\text{C15a})$$

$$\mathbf{Q}_{\text{HS}}^{\text{per}}(\mathbf{r}_1, \mathbf{r}_2) = -\frac{3\sqrt{2}}{\pi H^3} z_2(H - z_2) \sum_{m=-1,1} m' \tilde{S}_{\text{cyl}}^{+-}(\boldsymbol{\rho}_{12}; 0 \mid m') \hat{\mathbf{e}}_{m'}^*. \quad (\text{C15b})$$

The sums in (C15) can be evaluated explicitly using expressions (C7), (C13), and (15),

$$\begin{aligned} \mathbf{T}_{\text{HS}}^{\text{per}}(\mathbf{r}_1, \mathbf{r}_2) &= \frac{3}{2\eta H^3 L_x L_y} z_1(H - z_1)z_2(H - z_2) \mathbf{l}_{\parallel} + \sum_{\mathbf{n}} \Gamma(2, \pi\sigma^{-2}|\boldsymbol{\rho}_{12} - \boldsymbol{\rho}_{\mathbf{n}}|^2) \mathbf{T}_{\text{HS}}(\boldsymbol{\rho}_{12} - \boldsymbol{\rho}_{\mathbf{n}}; z_1, z_2) \\ &\quad - \frac{4\pi}{L_x L_y} \sum_{\mathbf{n} \neq 0} k_{\mathbf{n}}^2 \mathbf{T}_{\text{HS}}(\mathbf{k}_{\mathbf{n}}; z_1, z_2) \exp(-\pi\sigma^2 k_{\mathbf{n}}^2 + 2\pi i \boldsymbol{\rho}_{12} \cdot \mathbf{k}_{\mathbf{n}}), \end{aligned} \quad (\text{C16a})$$

$$\mathbf{Q}_{\text{HS}}^{\text{per}}(\mathbf{r}_1, \mathbf{r}_2) = \sum_{\mathbf{n}} \Gamma(1, \pi\sigma^{-2}|\boldsymbol{\rho}_{12} - \boldsymbol{\rho}_{\mathbf{n}}|^2) \mathbf{Q}_{\text{HS}}(\boldsymbol{\rho}_{12} - \boldsymbol{\rho}_{\mathbf{n}}; z_2) + \frac{2i}{L_x L_y} \sum_{\mathbf{n} \neq 0} \mathbf{Q}_{\text{HS}}(\mathbf{k}_{\mathbf{n}}; z_2) \exp(-\pi\sigma^2 k_{\mathbf{n}}^2 + 2\pi i \boldsymbol{\rho}_{12} \cdot \mathbf{k}_{\mathbf{n}}), \quad (\text{C16b})$$

where we have introduced notation

$$\mathbf{T}_{\text{HS}}(\boldsymbol{\rho}_{12}; z_1, z_2) = \mathbf{T}_{\text{HS}}(\mathbf{r}_1, \mathbf{r}_2), \quad (\text{C17a})$$

$$\mathbf{Q}_{\text{HS}}(\boldsymbol{\rho}_{12}; z_1, z_2) = \mathbf{Q}_{\text{HS}}(\mathbf{r}_1, \mathbf{r}_2). \quad (\text{C17b})$$

The quickly convergent Ewald sums (C16) can be used for efficient evaluation of the periodic Green's functions $\mathbf{T}_{\text{HS}}^{\text{per}}$ and $\mathbf{Q}_{\text{HS}}^{\text{per}}$ in Stokesian-dynamics and boundary-integral applications.

b. Matrix elements

The projections

$$G_{\text{HS}}^{\text{per}}(lm\sigma; \mathbf{r}_1 | l'm'\sigma'; \mathbf{r}_2) = \langle \mathbf{w}_{lm\sigma}^+(\mathbf{r}_1) | \mathbf{T}_{\text{HS}}^{\text{per}} | \mathbf{w}_{l'm'\sigma'}^+(\mathbf{r}_2) \rangle, \quad (C18)$$

of the periodic Hele–Shaw Green’s function $\mathbf{T}_{\text{HS}}^{\text{per}}$ onto the 3D spherical basis can be obtained using relation (C12) and applying the method described in [49]. The results can be written in the form analogous to Eq. (46) in Ref. [23],

$$G_{\text{HS}}^{\text{per}}(lm\sigma; \mathbf{r}_1 | l'm'\sigma'; \mathbf{r}_2) = -\frac{6}{\pi\eta H^3} C(Z_1; lm\sigma) \tilde{S}_{\text{cyl}}^{+-}(\boldsymbol{\rho}_{12}; m | m') C(Z_2; l'm'\sigma'). \quad (C19)$$

-
- [1] M. E. Staben, A. Z. Zinchenko, and R. H. Davis, “Motion of a particle between two parallel plane walls in low-Reynolds-number Poiseuille flow,” *Phys. Fluids* **15**, 1711–33 (2003).
- [2] R. B. Jones, “Spherical particle in Poiseuille flow between planar walls,” *J. Chem. Phys.* **121**, 483–500 (2004).
- [3] S. Bhattacharya, J. Bławdziewicz, and E. Wajnryb, “Hydrodynamic interactions of spherical particles in suspensions confined between two planar walls,” *J. Fluid Mech.* **541**, 263–292 (2005).
- [4] S. Bhattacharya, J. Bławdziewicz, and E. Wajnryb, “Many-particle hydrodynamic interactions in parallel-wall geometry: Cartesian-representation method,” *Physica A* **356**, 294–340 (2005).
- [5] S. Bhattacharya, J. Bławdziewicz, and E. Wajnryb, “Hydrodynamic interactions of spherical particles in Poiseuille flow between two parallel walls,” *Phys. Fluids* **18**, 053301 (2006).
- [6] M. E. Staben, A. Z. Zinchenko, and R. H. Davis, “Dynamic simulation of spheroid motion between two parallel plane walls in low-Reynolds-number Poiseuille flow,” *J. Fluid Mech.* **553**, 187–226 (2006).
- [7] Y. Han, A. Alsayed, M. Nobili, J. Zhang, T. C. Lubensky, and A. G. Yodh, “Brownian Motion of an ellipsoid,” *Science* **314**, 626–630 (2006).
- [8] M. Zurita-Gotor, J. Bławdziewicz, and E. Wajnryb, “Motion of a rod-like particle between parallel walls with application to suspension rheology,” *J. Rheol.* **51**, 71–97 (2007).
- [9] J. Pathak and K. B. Migler, “Droplet-string deformation and stability during microconfined shear flow,” *Langmuir* **19**, 8667–8674 (2003).
- [10] V. Sibillo, G. Pasquariello, M. Simeone, C. V., and S. Guido, “Drop deformation in microconfined shear flow,” *Phys. Rev. Lett.* **97**, Art. No. 054502 (2006).
- [11] A. J. Griggs, A. Z. Zinchenko, and R. H. Davis, “Low-Reynolds-number motion of a deformable drop between two parallel plane walls,” *Int. J. Multiphase Flow* **33**, 182–206 (2007).
- [12] P. J. A. Janssen and P. D. Anderson, “Boundary-integral method for drop deformation between parallel plates,” *Phys. Fluids* **19**, Art. No. 043602 (2007).
- [13] Y. L. Chen, M. D. Graham, J. J. de Pablo, G. C. Randall, M. Gupta, and P. S. Doyle, “Conformation and dynamics of single DNA molecules in parallel-plate slit microchannels,” *Phys. Rev. E* **70**, 060901(R) (2004).
- [14] O. B. Usta, J. Butler, and A. J. C. Ladd, “Transverse migration of a confined polymer driven by an external force,” *Phys. Rev. Lett.* **98**, 098301 (2007).
- [15] R. M. Jendrejack, D. C. Schwartz, J. J. de Pablo, and M. D. Graham, “Shear-induced migration in flowing polymer solutions: Simulation of long-chain DNA in microchannels,” *J. Chem. Phys.* **120**, 2513–2529 (2004).
- [16] R. Khare, M. D. Graham, and J. J. de Pablo, “Cross-stream migration of flexible molecules in a nanochannel,” *Phys. Rev. Letters* **96**, Art. No. 224505 (2006).
- [17] J. P. Hernández-Ortiz, J. J. de Pablo, and M. D. Graham, “N log N method for hydrodynamic interactions of confined polymer systems: Brownian dynamics,” *J. Chem. Phys.* **125**, 164906 (2006).
- [18] M. Zurita-Gotor, J. Bławdziewicz, and E. Wajnryb, “Swapping trajectories: a new wall-induced cross-streamline particle migration mechanism in a dilute suspension of spheres,” *J. Fluid Mech.* **592**, 447–469 (2007).
- [19] T. Beatus, T. Tlustý, and R. Bar-Ziv, “Phonons in a one-dimensional microfluidic crystal,” *Nature Phys.* **2**, 743–748 (2006).
- [20] M. Baron, J. Bławdziewicz, and E. Wajnryb, “Hydrodynamic crystals: collective dynamics of regular arrays of spherical particles in a parallel-wall channel,” *Phys. Rev. Lett.* **100**, 028001 (2008).
- [21] A. Alvarez, E. Clement, and R. Soto, “Confined suspension jet and long-range hydrodynamic interactions: A destabilization scenario,” *Phys. Fluids* **18**, 083301 (2006).
- [22] B. Cui, H. Diamant, B. Lin, and S. A. Rice, “Anomalous hydrodynamic interaction in a quasi-two-dimensional suspension,” *Phys. Rev. Lett.* **92**, 258301–1–4 (2004).
- [23] S. Bhattacharya, J. Bławdziewicz, and E. Wajnryb, “Far-field approximation for hydrodynamic interactions in parallel-wall geometry,” *J. Comput. Phys.* **212**, 718–738 (2006).
- [24] N. Liron and S. Mochon, “Stokes flow for a stokeslet between two parallel flat plates,” *J. Engineering Math.* **10**, 287–303 (1976).
- [25] S. Bhattacharya and J. Bławdziewicz, “Effect of small particles on the near-wall dynamics of a large particle in a highly bidisperse colloidal solution,” *J. Chem. Phys.*

- 128, 214704 (2008).
- [26] S. Bhattacharya and J. Bławdziewicz, “Image system for Stokes-flow singularity between two parallel planar walls,” *J. Math. Phys.* **43**, 5720–31 (2002).
 - [27] For a single spherical particle, the system has a cylindrical symmetry, and the two-dimensional tensors μ^{AB} can be replaced with scalar coefficients. However, tensorial notation is needed for multiparticle configurations and for systems of non-spherical particles.
 - [28] W. D. Jackson, *Classical Electrodynamics* (Wiley, New York, 1999).
 - [29] Calculations based on closely related ideas were reported in [19] and [21]. In particular, in the approach of [19] the particles (or drops) were modelled as disk-like objects. The magnitude of the scattered flow was estimated using the Hele–Shaw approximation combined with the volume conservation constraint, and the particle mobility remained an adjustable parameter (which was evaluated experimentally). The validity range of the single scattering approximation is discussed in [20].
 - [30] R. G. Cox and H. Brenner, “Effect of finite boundaries on Stokes resistance of an arbitrary particle. 3. Translation and rotation,” *J. Fluid Mech.* **28**, 391 (1967).
 - [31] P. Mazur and D. Bedeaux, “A generalization of Faxén’s theorem to nonsteady motion of a sphere through an incompressible fluid in arbitrary flow,” *Physica* **76**, 235–46 (1974).
 - [32] B. U. Felderhof, “Force Density Induced on a Sphere in Linear Hydrodynamics. II. Moving Sphere, Mixed Boundary Conditions,” *Physica A* **84**, 569–576 (1976).
 - [33] B. Cichocki, B. U. Felderhof, and R. Schmitz, “Hydrodynamic Interactions Between Two Spherical Particles,” *PhysicoChem. Hyd.* **10**, 383–403 (1988).
 - [34] The notation in Eq. (23a) is slightly different than the one used in our previous publications [3–5, 23], because the factor $a^{-2}\delta(\mathbf{r}_i - \mathbf{a})$ is now included in the basis function $\mathbf{w}_{lm\sigma}^+$. Otherwise, the normalization of the basis fields is the same as the one used in [3, 4].
 - [35] R. Shankar, *Principles of Quantum Mechanics* (Plenum, New York, 2008).
 - [36] S. Kim and S. J. Karrila, *Microhydrodynamics: Principles and Selected Applications* (Butterworth-Heinemann, London, 1991).
 - [37] J. Bławdziewicz, E. Wajnryb, J. A. Given, and J. B. Hubbard, “Sharp scalar and tensor bounds on the hydrodynamic friction and mobility of arbitrarily shaped bodies in Stokes flow,” *Phys. Fluids* **17**, 033602–1–9 (2005).
 - [38] W. W. Hackborn, “Asymmetric Stokes flow between parallel planes due to a rotlet,” *J. Fluid Mech.* **218**, 531–46 (1990).
 - [39] Strictly speaking, for $m = \pm 1$ the lattice sums (54) are not absolutely convergent. However, Eqs. (55) and (56) yield a unique definition of the functions $\mathbf{T}_{\text{HS}}^{\text{per}}$ and $\mathbf{Q}_{\text{HS}}^{\text{per}}$.
 - [40] D. Frenkel and B. Smit, *Understanding Molecular Simulation. From Algorithms to Simulations* (Academic Press, New York, 2002).
 - [41] B. Cichocki and B. U. Felderhof, “Electrostatic interactions in two-dimensional Coulomb systems with periodic boundary conditions,” *Physica A* **158**, 706–22 (1989).
 - [42] K. E. Sung, S. A. Vanapalli, D. Mukhija, H. A. McKay, J. Mirecki-Millunchick, M. A. Burns, and M. J. Solomon, “Programmable Fluidic Production of Microparticles with Configurable Anisotropy,” *J. Am. Chem. Soc.* **130**, 1335–1340 (2008).
 - [43] N. Lecoq, R. Anthore, B. Cichocki, P. Szymczak, and F. Feuillebois, “Drag force on a sphere moving towards a corrugated wall,” *J. Fluid Mech.* **513**, 247–264 (2004).
 - [44] O. I. Vinogradova and G. E. Yakubov, “Surface roughness and hydrodynamic boundary conditions,” *Phys. Rev. E* **73**, Art. No. 045302 (2006).
 - [45] S. Bhattacharya, “Cooperative motion of spheres arranged in periodic grids between two parallel walls,” *J. Chem. Phys.* **128**, 074709 (2008).
 - [46] T. Thusty, “Screening by symmetry of long-range hydrodynamic interactions of polymers confined in sheets,” *Macromolecules* **39**, 3927–3930 (2006).
 - [47] A. Balducci, M. P., J. Y. Han, and P. S. Doyle, “Double-stranded DNA diffusion in slitlike nanochannels,” *Macromolecules* **39**, 6273–6281 (2006).
 - [48] A. R. Edmonds, *Angular Momentum in Quantum Mechanics* (Princeton University Press, Princeton, 1960).
 - [49] S. Bhattacharya, “Hydrodynamic interactions in confined geometries,” Ph.D. thesis, Yale University, 2005.